# The Ice, Cloud, and Land Elevation Satellite – 2 Mission: A Global Geolocated Photon Product Derived From the Advanced Topographic Laser Altimeter System

Thomas A. Neumann[a], Anthony J. Martino[a], Thorsten Markus[a], Sungkoo Bae[b], Megan R. Bock[a,c], Anita C. Brenner[a,d], Kelly M. Brunt[a,e], John Cavanaugh[a], Stanley T. Fernandes[f], David W. Hancock[a,g], Kaitlin Harbeck[a,g], Jeffrey Lee[a,g], Nathan T. Kurtz[a], Philip J. Luers[a], Scott B. Luthcke[a], Lori Magruder[b], Teresa A. Pennington[a,g], Luis Ramos-Izquierdo[a], Timothy Rebold[a,h], Jonah Skoog[f], Taylor C. Thomas[a,h]

[a] NASA Goddard Space Flight Center, Greenbelt, MD United States

[b] Applied Research Laboratory, University of Texas, Austin, TX United States

[c] ADNET Systems, Inc., Lanham, MD United States

[d] Sigma Space Corporation, Lanham, MD United States

[e] University of Maryland, College Park, MD United States

[f] Northrop Grumman Innovation Systems, Gilbert, AZ United States

[g] KBR, Greenbelt, MD United States

[h] Emergent Space Technologies, Laurel, MD United States

## Abstract

The Ice, Cloud, and land Elevation Satellite – 2 (ICESat-2) observatory was launched on 15 September 2018 to measure ice sheet and glacier elevation change, sea ice freeboard, and enable the determination of the heights of Earth's forests. ICESat-2's laser altimeter, the Advanced Topographic Laser Altimeter System (ATLAS) uses green (532 nm) laser light and single-photon sensitive detection to measure time of flight and subsequently surface height along each of its six beams. In this paper, we describe the major components of ATLAS, including the transmitter, the receiver and the components of the timing system. We present the major components of the ICESat-2 observatory, including the Global Positioning System, star trackers and inertial measurement unit. The ICESat-2 Level 1B data product (ATL02) provides the precise photon round-trip time of flight, among other data. The ICESat-2 Level 2A data product (ATL03) combines the photon times of flight with the observatory position and attitude to determine the geodetic location (i.e. the latitude, longitude and height) of the ground bounce point of photons detected by ATLAS. The ATL03 data product is used by higher-level (Level 3A) surface-specific data products to determine glacier and ice sheet height, sea ice freeboard, vegetation canopy height, ocean surface topography, and inland water body height.

**Highlights**

- Describes the ICESat-2 Observatory and its sole instrument: the Advanced Topographic Laser Altimeter System (ATLAS)
- Presents the structure and major contents of the ICESat-2 Level 1B data product (ATL02; photon times of flight)
- Presents the structure and major contents of the ICESat-2 Level 2A data product (ATL03; Global Geolocated Photons)

## 1. Introduction

The National Aeronautics and Space Administration (NASA) launched the Ice, Cloud, and Land Elevation Satellite – 2 (ICESat-2) mission on 15 September 2018 to measure changes in land ice elevation and sea-ice freeboard, and enable determination of vegetation canopy height globally (Markus et al., 2017). A follow-on of the ICESat laser altimetry mission was recommended by the National Research Council (National Research Council, 2007). Thus, ICESat-2 builds upon the heritage of the ICESat mission (Zwally et al., 2002; Schutz et al., 2005) and uses round-trip travel time of laser light from the observatory to Earth as the fundamental measurement. During the development of mission objectives and requirements, the science community made clear from lessons learned that duplication of ICESat would not suffice. The science objectives for ICESat-2 are as follows:

*-Quantify polar ice-sheet contributions to current and recent sea-level change and the linkages to climate conditions;*

*-Quantify regional signatures of ice-sheet changes to assess mechanisms driving those changes and improve predictive ice sheet models; this includes quantifying the regional evolution of ice-sheet change, such as how changes at outlet glacier termini propagate inward;*

*-Estimate sea-ice thickness to examine ice/ocean/atmosphere exchanges of energy, mass and moisture;*

*-Measure vegetation canopy height as a basis for estimating large-scale biomass and biomass change.*

The first objective corresponds to ICESat's sole science objective. Results from ICESat, however, showed that an ICESat follow-on must allow researchers to readily distinguish elevation change from the elevation uncertainty due to imperfect pointing control over the outlet glaciers along the margins of Greenland and Antarctica because those areas are where changes are the most rapid. This requirement led to the formulation of the second objective, which strongly directed the ICESat-2 science requirements and the design of the mission. For example, ICESat-2 needed multiple beams in order to monitor those rapidly changing regions with the necessary accuracy and precision. The traceability from science objectives to science requirements and subsequently to mission design and implementation is discussed in detail in Markus et al. (2017). Furthermore, results from ICESat proved that spaceborne laser altimetry is sufficiently precise to retrieve sea-ice freeboard and ultimately calculate sea-ice thickness. Consequently, the determination of the sea-ice thickness is an official science objective for ICESat-2. Because only 1/10th of the sea ice thickness is above sea level, this objective was the driver for much of the vertical precision requirements such as timing as discussed in Markus et al. (2017).

Because much of the mission design, and vertical and horizontal accuracy and precision requirements, are driven by the land- and sea-ice scientific objectives, the fourth objective exists largely to ensure that ICESat-2 is collecting, processing, and archiving scientifically viable data around the globe.

The sole instrument on the ICESat-2 observatory is the Advanced Topographic Laser Altimeter System (ATLAS). In designing ATLAS, close attention was paid to the successes and limitations of the GLAS (Geoscience Laser Altimeter System) instrument flown on the original ICESat mission (Abshire et al., 2005; Webb et al., 2012). Both lidars were designed, assembled, and tested at NASA Goddard Space Flight Center, bringing substantial heritage and insight forward to the ICESat-2 mission and ATLAS.

ATLAS splits a single output laser pulse into six beams (arranged into three pairs of beams) of low-pulse energy green (532 nm) laser light at a pulse repetition frequency (PRF) of 10 kHz. The arrangement of pairs of beams allows for measurement of the surface slope in both the along- and across-track directions with a single pass, enabling determination of height change from any two passes over the same site. The single-photon sensitive detection strategy (Degnan, 2002) allows individual photon times of flight (TOF) to be determined with a precision of 800 picoseconds.

The footprint size of the laser on the ground is ~17 m. The small footprint size together with the TOF and PRF requirements ensure that sea surface height measurements within sea-ice leads have a vertical precision of 3 cm. The resulting height measurements can be aggregated in order to meet the overall ICESat-2 science requirements (Markus et al., 2017). To determine the pointing direction of ATLAS, the ICESat-2 observatory carries state-of-the-art star trackers and an inertial measurement unit (IMU) mounted on the ATLAS optical bench. To determine the 3-D position of the observatory center of mass, the observatory also carries redundant dual-frequency Global Positioning System (GPS) systems. The ATLAS TOF data are combined with the observatory position and attitude to produce a geolocation for each photon in the resulting data product.

The ICESat-2 Science Unit Converted Telemetry Level 1B data product (identified as ATL02; Martino et al., 2018) provides the ATLAS TOF, ATLAS housekeeping data, and the other data necessary for science data processing such as GPS and attitude data. The ICESat-2 Global Geolocated Photon Level 2A data product (identified as ATL03; Neumann et al., 2018) provides the latitude, longitude and ellipsoidal height of photons detected by the ATLAS instrument. The ATL03 product is used as the foundation for other surface-specific geophysical data products such as sea ice (ATL07; Kwok et al., 2016), land ice (ATL06; Smith et al., this issue), and vegetation canopy height (ATL08; Neuenschwander and Pitts, in review). All ICESat-2 data products are provided in the Hierarchical Data Format – version 5 (HDF-5) format and will be made available through the National Snow and Ice Data Center (NSIDC - https://nsidc.org/data/icesat-2).

In this paper, we describe the ICESat-2 observatory, the major systems of the ATLAS instrument, including the components of the transmitter, receiver, the timing system and active alignment subsystems. The approach to monitoring the internal range bias of ATLAS is described, along with other major features of the primary ATLAS data. We also review the anticipated radiometric performance and timing precision of ATLAS. We summarize the components of the spacecraft bus that are relevant to the ICESat-2 data products and performance. We combine these primary outputs of the ICESat-2 observatory into an overview of the two low level data products: the Level 1B product (ATL02), and the Level 2A product (ATL03).

## 2. The ICESat-2 Observatory

The ICESat-2 mission consists of two major components: the observatory in space, and the ground system which downlinks data from the observatory and generates the ICESat-2 data product suite. The observatory (Figure 1) is composed of two components as well: the ATLAS instrument which is a lidar system and records photon arrival times; and the spacecraft bus which provides power, via solar arrays, the Global Positioning System (GPS) receivers and antennae and communications antennae among other instrumentation.

### 2.1 The ATLAS Instrument

The ATLAS instrument has three principal systems: the transmitter that generates the laser pulses, the receiver where photons are detected and timed, and the alignment monitoring and control system which includes the laser reference system (LRS) to determine the laser pointing direction. These systems together provide TOF, position and pointing that are needed to retrieve precise photon height estimates. Some of the major characteristics of the contributing systems are summarized in Table 1 and described in more detail below.

#### 2.1.1 Transmitter

The components of the ATLAS transmitter include: the lasers, the Laser Sampling Assembly, Beam Shaping Optics, the Beam Steering Mechanism (BSM), and the Diffractive Optical Element (Figure 2). ATLAS carries two lasers (primary and redundant), only one of which is active at a time. The Laser Sampling Assembly samples a portion of the transmitted light and routes it to the Start Pulse Detector, which times the outgoing laser pulse. The Beam Shaping Optics sets the beam divergence (i.e. the angular measure of the beam diameter as a function of distance from ATLAS) , while the BSM ensures that the transmitted beams are aligned with the fields of view of the receiver. Lastly, the Diffractive Optical Element splits the single outgoing beam into 6 beams.

The core of the ATLAS transmitter are the lasers, which were designed and fabricated by Fibertek, Inc. (Sawruk et al., 2015). Based on the requirements for a narrow pulse width (< 1.5 ns), variable pulse energy of up to 1.2 millijoule (mJ) (adjustable from 0.2 up to 1.2 mJ), and 10 kHz PRF, Fibertek designed a master oscillator / power amplifier (MOPA) based laser transmitter. The design uses a

Nd:$YVO_4$ gain crystal to generate infrared (1064 nm) light with the required pulse width, which is then frequency-doubled to produce green 532 nm laser light. Although the conversion to 532 nm reduces the overall laser efficiency compared with a 1064 nm transmitted beam, green light was selected based on the maturity of photon-sensitive detector technology for that wavelength. This selection minimized the overall risk and maximized the overall system throughput from transmitter to receiver. We expect the central wavelength of the laser (532.272 $\pm$ 0.15 nm) to change very slowly over time, if at all, due to aging effects. A single laser is expected to meet the nominal three-year mission duration, or approximately one trillion pulses.

After exiting the laser module, the outgoing beam from the operational laser travels along a common optical path after a polarizing beam combiner, and is sampled by the Laser Sampling Assembly, which removes < 1% of the outgoing beam energy to monitor the stability of the central wavelength as well as to provide the precise laser transmit time (described in Section 2.1.3). When coupled with the arrival time of returning photons, the laser transmit time enables the determination of TOF, the fundamental ATLAS measurement.

The outgoing beam is shaped by several optics (indicated by Beam Shaping Optics in Figure 2) to generate the required beam divergence giving a nominal footprint diameter of ~17 m at ICESat-2's 500 km average orbital altitude. The pointing vector of the laser beam is determined by the position of the BSM, which provides the means for active beam steering to ensure alignment with the receiver (further discussed in section 2.1.4). The BSM contains redundant hardware to mitigate against the risk of a mechanism failure.

The single output beam is split into six primary beams by the Diffractive Optical Element (DOE) prior to exiting the ATLAS instrument. As the light exits the DOE, all beam information (pointing direction, shape, strength) becomes beam-specific. As such, the DOE is the last common reference point of the six beams.

Approximately 80% of the laser pulse energy is partitioned into the six primary outgoing laser beams, while 20% is lost to higher-order modes. At the nominal laser power setting, this means that ~660 microjoules (μJ) of the ~835 μJ pulse is used, and ~175 μJ are lost to higher-order modes. The total available laser energy precluded the scenario of having six strong beams; as a result the six primary beams generated by the DOE have unequal energy, with three relatively strong beams and three relatively weak beams. Given the energy losses along the optical path in the laser transmission, the strong beams each contain ~21% of the transmitted energy (~175 μJ per pulse) and the weak beams share the remaining energy, each having ~5.2% (~ 45 μJ per pulse). As such, the energy ratio of the strong and weak beams is approximately 4:1. The strong and weak beams have transmit energy levels to within approximately 10% of the mean values (i.e. 175 ±17 μJ per pulse for the strong beams and 45 ±5 μJ per pulse for the weak beams).

The strong/weak configuration for the ATLAS beams was designed to enhance radiometric dynamic range, thus accommodating the disparate energy levels required to meet the primary science objectives (Markus et al., 2017). It is expected that both the strong and weak beams will provide sufficient signal-to-noise ratios for altimetry measurements over bright surfaces such as sea ice and ice sheets, while the strong beams will be the primary means for ranging to low-reflectivity targets, such as oceans and, at times, over vegetation (see section 2.2 for an outline of surface types).

In summary, the ATLAS transmitter will generate the six beams needed to achieve the multidisciplinary science objectives of the ICESat-2 mission. The transmitted pulses are narrow (<1.5 ns), use 532 nm laser light, and generate ~17 m diameter footprints on the ground. The combination of the laser PRF and spacecraft velocity of ~7 km/sec produce footprints on the ground spaced ~0.7 m along track, resulting in substantial overlap between shots. This represents a substantial improvement in along-track resolution over the ICESat mission, which generated non-overlapping footprints on the ground of ~70 m diameter spaced ~150 m along track. Over the first nine months of the mission, the ATLAS transmitter components are working on-orbit as designed and are performing as expected.

### 2.1.2 Receiver

Within the ATLAS receiver (Figure 3), light is collected and focused onto the receiver optics by the telescope. The figure, finish and coating of the telescope surface is optimized for transmission of green light.  The light from each of the six beams is focused onto fiber optic cables dedicated to each beam.  At ICESat-2's nominal altitude, this generates a 45 m diameter field of view on the ground (see section 2.1.4).  Background light is first rejected by pass band coarse filters, and then by optical etalon filters centered at the nominal laser output central wavelength.  The central wavelengths of both the transmitted laser beam as well as the pass band of the etalon filters are tunable over a 30 pm range by adjusting their respective temperatures via the ATLAS avionics system.  Feedback for this wavelength matching is provided by both the received signal strength and the Wavelength Tracking Optical and Electronics Module (WTOM/WTEM), which samples a fraction of the laser energy and directs it through an optical filter assembly that is identical to the receiver background filters. Based on pre-launch testing, we expect to retune the optical etalon filters on orbit approximately twice a year to match the laser transmit wavelength.

The output of the filters is fiber-coupled to one of two sets of single-photon sensitive photo-cathode array photomultiplier tubes (PMTs) in the detector modules which convert optical energy into electrical pulses (Figure 4).  ATLAS uses 16-element PMTs manufactured by Hamamatsu with pixels arranged in a 4x4 pattern.  Each channel of a single PMT is used independently for each of the three strong beams to provide 16 independent electrical outputs, while for the weak beams (which are ~ ¼ the optical power of the strong beams) detector channels are combined to a 2x2 array. As such, ATLAS has 60 electrical outputs which are mapped to 60 independent timing channels. Test data show that incoming light is distributed uniformly to each channel of a strong or weak beam (to within 10%), which is an important consideration for estimating detector gain during periods of high throughput. While we expect a single set of detectors to survive for the duration of the mission, ATLAS has a second set of redundant detectors. The switch from the primary to the redundant set of detectors is accomplished via a set of six moveable mirrors.

Overall, the optical throughput of the ATLAS receiver was measured to be 40% in pre-launch testing. Over the mission lifetime, we expect degradation of the ATLAS receiver throughput due to aging and contamination effects, and expect the end-of-life throughput to be greater than 35%. The efficiency of the PMTs in converting optical energy to electrical pulses has been measured to be ~15%, and the gain can be adjusted as needed by manipulating the bias voltage to maintain consistent performance throughout the mission. Combined, the overall efficiency of the ATLAS receiver is ~ 6%. Over the first nine months of the mission, the ATLAS receiver components are performing as designed.

### 2.1.3 Time of Flight Design

The electrical output of the detector timing channels are routed to photon-counting electronics (PCE) cards that enable precise timing of received photon events. ATLAS contains three PCE cards, each handling the output of a single strong beam (16 channels), a single weak beam (four channels) and two channels from the start pulse detector used for timing start pulses. The PCE cards are similar to those developed for the airborne Multiple Altimeter Beam Experimental Lidar (MABEL) instrument (McGill et al., 2013).

Each PCE card is sent times from a free-running 100 MHz clock to measure coarse times of photon arrivals at the ~10 ns level, and a chain of sequential delay cells is used to measure fine times at the 180-200 picosecond level. The transmitted data include the coarse and fine time components of events from each PCE and other data needed to cross-calibrate times between PCEs. A free-running counter driven by an Ultra Stable Oscillator (USO) is latched by the GPS 1 pulse per second signal from the spacecraft. The same free-running counter is latched by an internal 1 pulse per second signal. This allows the internal timing of ATLAS to be matched to the GPS time. The stability of the USO frequency is a primary consideration in estimating height change to meet the requirements of the mission (Markus et al., 2017), as drift in USO frequency has a first-order impact on our ability to precisely measure photon TOF. Ground processing uses these components to determine the absolute time of ATLAS events, including laser firing times and photon arrival times, to calculate round-trip TOF.

ATLAS uses on-board software to limit the number of time-tagged photon events and reduce the overall data volume telemetered to ground stations. A digital-elevation model (DEM), an estimate of the surface relief (Leigh et al., 2014), and a surface classification mask are used to constrain the time tags to those received photons most likely to have been reflected from Earth's surface. This window of time-tagged photons is called the Range Window. Individual ATLAS transmitted pulses are separated in flight by ~15 km; the vertical span of time-tagged photons varies from a maximum of 6 km over areas on Earth with substantial surface relief to a minimum of ~1 km over surfaces with minimal relief.  This narrower Range Window reduces the number of photons that ATLAS must time tag to search for the surface echoes of most interest.  The span of photon time tags is further reduced by forming histograms of photon time tags to statistically determine the photon events most likely reflected from the Earth's surface.  The span of photon time tags telemetered to ground (called the Telemetry Band or Bands) processing varies from up to 3 km over rugged mountain topography to ~40 m over the oceans, and the Telemetry Band width is re-evaluated every 200 pulses.

#### 2.1.4 Alignment and alignment monitoring

Owing to the tight tolerance between the receiver field of view for an individual beam and the diameter of a reflected laser beam, keeping the transmitted laser light within the receiver field of view is a primary challenge for ATLAS. The instrument's Alignment Monitoring and Control System (AMCS) (Figure 5) provides a means to evaluate the co-alignment between the transmitter and receiver.

The Telescope Alignment and Monitoring System (TAMS) consists of a LED source coupled to four fiber optics to generate a rectangular pattern of beams at the telescope focal plane.  These beams are projected from the focal plane through the telescope aperture.  A portion of these beams is sampled using a lateral transfer retroreflector (LTR) and routed to an imager on the laser side of the laser reference system (LRS) mounted on the optical bench. The resulting image of the TAMS spots enables determination of the telescope pointing vector. The pointing vector of the transmitted beams is provided by routing a small fraction (<< 1 %) of the transmitted energy for each of the six outgoing beams to the same imager using a second LTR. By comparing the relative positions of the TAMS spots and laser spots within the same image on the laser side of the LRS, the AMCS determines the relative alignment of the transmitter and receiver. If necessary, the AMCS generates corrections to the position of the BSM which adjusts the pointing vector for the laser beam prior to its separation into six beams by the DOE. To prevent potentially unstable corrections to the BSM position, the AMCS calculates the relative position of the TAMS and laser spots at a higher rate (50 Hz) than corrections to the BSM are commanded (10 Hz). Pre-launch data during whole-instrument testing has demonstrated that the AMCS is able to correct for short timescale perturbations (vibrations due to nearby activities, such as walking) as well as long timescale perturbations (such as thermal effects of clean room air conditioning on/off cycles). On orbit, the main driver of alignment change is the time-varying thermal condition of the ATLAS components both around an orbit and seasonally.

In the event that the AMCS system is not able to align the transmitted laser beams with the receiver fields of view for all six beams simultaneously, the radiometric throughput for those misaligned beams will be diminished. For a moderate degree of misalignment, some fraction of the returning laser pulse will be clipped and the number of photons collected by the ATLAS telescope will be reduced. Those photons that do enter the receiver field of view will be biased to one side of the field of view. The net effect will be to reduce the surface height precision for those beams affected, owing to a reduced number of signal photons available for further analysis. The limiting case would be a total loss of overlap between the returning photons and the receiver field of view. In this case the photon loss is total, and these beams would not be used in further data processing. Over the first nine months of the mission, we have found no evidence of photon loss due to misalignment in our initial on-orbit data.

While the AMCS provides routine corrections to the transmit and receive alignment algorithm, we also will conduct periodic calibration scans of the BSM to systematically sweep the transmitted laser beams across the receiver fields of view to determine a new center position. Since the BSM steers all six beams simultaneously it may not be possible to perfectly center all six beams simultaneously within their respective fields of view. In such an event, the BSM position will be optimized to capture the maximum number of returned photons across all six beams, using data from the BSM calibration scans. We have conducted such scans frequently during ATLAS commissioning during the first 60 days on orbit, and will do so as needed thereafter during nominal operations. Over the first nine months of the mission, the ATLAS alignment has been very stable, with BSM changes on the order of a few (< 10) microradians. At the nominal altitude, this represents a movement of the laser spots by about 1/3 the diameter of the laser footprints.

### 2.1.5 Time of flight bias and bias monitoring

While the primary purpose of ATLAS is to measure photon round-trip time of flight, meeting the high-precision height measurement requirements (Markus et al., 2017) requires close attention to and correction for internal timing drifts within ATLAS. Prior to launch, a rigorous testing program characterized the range difference between beams to a fixed target in ambient conditions, as well as during thermal-vacuum testing for a range of instrument states. This testing determined that the range reported by ATLAS will vary by less than a millimeter depending on the instrument state and temperature. On orbit, the Transmitter Echo Path (TEP) provides a means to monitor time-of-flight changes within ATLAS.

The TEP routes a portion of the light used to measure the time of the start pulse from the start pulse detector into the receive path just prior to the optical filters for two of the strong beams (ATLAS beams 1 and 3). The optical power in this internal pathway is small, amounting to approximately one photon every ~20 laser transmit pulses. The TEP photons have a time of flight of approximately 20 nanoseconds given the length of the fiber optics that provide the pathway from the start pulse detector. Monitoring changes in the distribution of TEP-based photons over time can reveal changes in the ATLAS reported time of flight (i.e. a range bias change). The path traversed by the TEP photons include the aspects of ATLAS we expect to be most sensitive to temperature changes and ageing effects (e.g. the PMTs and electrical pathways). While it is possible that changes in the transmit or receive optics not sampled by the TEP could cause changes in the reported photon time of flight, a change in the position of such components by more than a few hundredths of a millimeter would likely be due to some catastrophic change (e.g. a broken or unbounded optic).

Photons travel along the TEP any time the laser is transmitting. At times, the TEP-based photons will arrive within the range window where the on-board software is searching for surface-reflected photons. In this circumstance, ATLAS will telemeter the TEP-based photon data along with the surface-reflected photon data, and ground processing will assign them to the correct start pulse to yield a ~20 nanosecond time of flight (as opposed to a ~3.3 millisecond time of flight for surface-reflected photons). We expect TEP-based photons to arrive at nearly the same time as photons reflected from the Earth approximately twice per orbit. Although this will not impact nominal science operation, ATLAS can be commanded to telemeter only TEP-based photons during calibration activities. Using TEP-based photons, we will characterize the changes in ATLAS range bias throughout one or more orbits early in the mission, and repeat this calibration periodically as needed.

TEP-based photons also sample a substantial fraction of the components contributing to the ATLAS impulse-response function (see section 4.6 for a detailed description). By aggregating TEP-based photons, an estimate of this function can be constructed in ground processing, and changes in this function can be monitored.

#### 2.1.6 Dead time

The full waveform GLAS altimeter instrument onboard ICESat was susceptible to detector saturation in those cases where relatively high-energy return pulses overwhelmed the capability of the automatic gain control on the 1064 nm detectors (Sun et al., 2017). The resulting saturation led to returned waveforms that were either clipped or artificially wide (Fricker et al., 2005). While the PMT detector elements do not suffer from saturation, they are discrete detectors and therefore susceptible to dead-time effects (Williamson et al., 1988; Sharma and Walker, 1992). Dead time is the time period after a detected photon event during which the detector is unable to detect another photon event. This means that a photon arriving in close temporal proximity to a prior photon event will not be detected. In some cases, during periods of high throughput, a detector channel remains blind to subsequent photon arrivals if those additional photons arrive at the same channel during the dead time period, thus extending the effective dead time, perhaps significantly.

ATLAS has three features which are each intended to partially mitigate the dead time effect. First, the ATLAS PMTs are 16-pixel photo-cathode array PMTs. By distributing the light uniformly across the detector pixels (16 unique pixels for each strong beam; four unique pixels for each weak beam; Figure 4), this design reduces the probability that dead time effects will be realized. Second, ATLAS uses a dead time circuit to limit the pulse interarrival time in a timing channel to greater than 3 ns (nominally 3.2 ns), so as to avoid hardware-specific dead times that could be different among channels. Third, the corresponding beam and detector channel that recorded each detected photon is preserved in the telemetered data. Consequently, it is possible to monitor the effective gain of the pixels in a given beam to estimate the probability and magnitude of dead time effects. Pre-launch data with a range of photon inter-arrival times have been used to estimate the radiometric and ranging degradation of ATLAS due to dead time effects. This functionality has proven to be useful in characterizing ATLAS' initial on-orbit performance.

## 2.2 Expected ATLAS performance

Despite the narrow bandpass filtering implemented on ATLAS to constrain the received light to 532.272 ± 0.15 nm, there remains a significant amount of sunlight at that wavelength when ATLAS is ranging to the sun-lit Earth. These solar background photons are reflected off the Earth's surface, and some fraction of them enter the ATLAS telescope and are recorded by the receiver electronics. The rate of background photons recorded by ATLAS varies primarily with the sun angle, but also with the atmospheric and Earth reflectivity at 532 nm. In regions with high solar angle and reflectance, background photon rates of ~10 MHz have been measured (or 10 million background photons per second; or about 1 photon every 3 m in height) for any given beam; the rate at any specific location will be a function of the reflectance in the ATLAS field of view and solar angle. The ~10 MHz value is observed with clear skies over the ice sheet interior in summer. The presence of background photons increases the expected standard deviation of the return pulse from the ice sheet interior by about 50% to ~2.5 cm and ~5 cm for the strong and weak beams, respectively (Markus et al., 2017, Table 1).

We developed a variety of design cases based on targets of interest to predict the ability of the ATLAS instrument to provide data with sufficient precision and accuracy to satisfy the mission science requirements (Markus et al., 2017). During ATLAS design and testing, these design cases were used as a benchmark to evaluate the ATLAS timing and radiometric performance. The number of signal photons expected per shot is a function of the surface reflectance and losses in the atmosphere combined with the ATLAS radiometric model. The temporal distribution of the returned photons is primarily a function of the interaction of the transmitted pulse (~1.5 ns pulse width) with the surface slope and roughness over the laser footprint area both of which broaden the return pulse. In addition, the surface reflectance and atmospheric optical depth have a first-order effect on the number of returned signal photons per shot. Over relatively flat reflective surfaces, such as the interior of the Antarctic ice sheet (surface reflectance 0.9; optical depth of atmosphere 0.21), we expect ~7 signal photons per shot for the strong beams and ~1.75 signal photons per shot for the weak beams on average. Due to the relatively flat and smooth ice sheet interior, we expect little pulse spreading or slope-induced geolocation error, leading to a standard deviation of the signal photons averaged over 100 shots of ~1.5 cm and ~2.8 cm for the strong and weak beams respectively.

Over low reflectivity targets, such as ocean water, both the signal photon rates and background photon rates are significantly reduced. For the dark ocean water in sea ice leads (i.e. the gaps between highly reflective sea ice where ocean water is visible;

surface reflectance 0.2; optical depth 0.4), we expect ~0.2 and ~0.05 signal photons per shot for the strong and weak beams respectively. In the summer, our modeling predicts a background rate of ~4 MHz. Under these conditions, the standard deviation of the returned photons for 100 shots will be ~3 cm and ~5 cm for the strong and weak beams, respectively (Markus et al., 2017, Table 1). After the first few months of on-orbit operation, the ATLAS signal photon rate and background photon rates are consistent with pre-launch expectations. We will continue to monitor the ATLAS radiometric performance throughout the life of the mission.

Significant topographic relief within a laser footprint broadens the return pulse and increases the standard deviation of the signal photon distribution. Over outlet glaciers, assuming a surface slope of 4 degrees, surface roughness of 2 m RMS, and a surface reflectance of 60% in the summer months with an optical depth of 0.6, we predict receiving ~3 signal photons for the strong beams and ~0.6 signal photons for the weak. Given a background photon rate of 8 MHz in this scenario, we predict a standard deviation of the signal photon distribution ~10 cm and ~20 cm for the strong and weak beams respectively (Markus et al., 2017, Table 1).

### 2.3 The ICESat-2 Spacecraft Bus

The ICESat-2 spacecraft bus was provided by Northup-Grumman Innovation Systems in Gilbert, AZ and includes the X- and S-band antennas needed to transmit data and commands between the observatory and the ground system, the solar array and batteries needed to power the ATLAS instrument, the GPS receivers and antennas, as well as the necessary hardware for adjusting the observatory attitude and altitude. Additional components typically on the spacecraft bus (such as the star trackers and IMU) are mounted on the ATLAS optical bench, as noted above.

The GPS hardware on the ICESat-2 spacecraft bus was developed and provided by RUAG Holding AG, which has supplied similar systems for the European Space Agency's Sentinel missions (Montenbruck et al., 2017) among others. The ICESat-2 spacecraft carries redundant GPS receivers and antennas to mitigate against single-point failures. These data are the primary input to the precision orbit determination, described in more detail below. In addition, the spacecraft carries a nadir-mounted retroreflector for satellite laser ranging for orbit verification (Pearlman et al., 2002).

The Instrument Mounted Spacecraft Components (IMSC) assembly is mounted to the ATLAS optical bench. The IMSC has two HYDRA star tracker optical heads provided by Sodern (Blarre et al., 2010) that have been used on many spacecraft (e.g. ESA's Sentinel missions). Each HYDRA optical head has a 16x16 degree field of view focused on a 1024x1024 pixel Active Pixel Sensor (CMOS) detector. The heads operate concurrently at 10Hz, tracking up to 15 stars each, and communicate with a separate star tracker electronics unit mounted on the Spacecraft bus. Attitude data supplied by the optical heads is processed with the data provided by a Northrop Grumman Scalable Space Inertial Reference Unit (SSIRU) to determine the observatory attitude, and ultimately, the pointing vector for each of the six ATLAS beams, as described below. The SSIRU comprises four Hemispherical Resonator

Gyros in a 3-for-4 redundant pyramid arrangement, along with redundant Processor Power Supply Module boards. The SSIRU has exceptional bias and alignment stability as well as low noise, which are critical to meeting ICESat-2 attitude estimation performance requirements.

## 3. The ATL02 Data Product: Science Unit Converted Telemetry

The ATL02 data product (Martino et al., 2018) converts the low-level telemetry from the observatory and applies calibrations to the primary photon data to generate precise photon times of flight. The ATL02 data product includes separate groups for possible TEP photons, housekeeping temperatures and voltages from ATLAS, and the data necessary to determine the pointing direction of the ATLAS laser beams (e.g. data from the GPS, LRS, and star trackers). In the ATL02 data structure, the /atlas group contains the science data of interest to most users. The altimetry data (such as photon time of flight) is organized according to PCE card into the /atlas/pcex subgroups, where x refers to the pce card number. The /atlas/pcex/algorithm_science group contains the data used for precise time of day and data alignment between s the three PCE cards. The groups /gpsr, /lrs, and /sc contain data used to determine the precise orbit and pointing vectors of the ATLAS laser beams.

### 3.1 Time of flight

As noted above, each of the three PCE cards use two timing channels to record start pulse information. The transmit pulse generated by ATLAS has a full-width at half maximum duration of less than 1.5 nanoseconds (Sawruk et al., 2015) but is slightly asymmetric. To account for this asymmetry, and possible changes in the pulse skew through time, ATLAS measures the time that the laser pulse crosses two energy thresholds on the rising and falling edges of the transmit pulse, as depicted in Figure 6. The time that the transmit pulse crosses the leading lower threshold is recorded by each of the three PCEs, and provides a means to cross-calibrate times among the PCEs. In addition, each PCE records one of the remaining three times (leading edge upper threshold, falling edge upper threshold, or falling edge lower threshold). In ground processing, these 6 times are combined to calculate the centroid of the four crossing times, after co-aligning the times using the leading lower threshold crossing time for each PCE to produce a single start time for each pulse.

The combination of ICESat-2's orbit altitude and the laser transmitter PRF results in ~30 transmitted and reflected laser pulses in transit to and from the observatory at any given time. The precise number of pulses in flight depends on a combination of the orbit altitude and Earth's topography at a given location. Consequently, the times of transmitted laser pulses and received photon time tags must be aligned in ground processing before a precise time-of-flight of any given photon can be determined. Errors in this time alignment would manifest as ~15 km errors in the reported range and are relatively easily detected in post-processing analysis. A consequence of the spacing of transmit pulses in flight is that reflections from high clouds in the atmosphere above 15 km can be folded into the ground return; e.g. there is a height ambiguity between returns from 16 km above the surface and 1 km above the surface.

In addition to the timing processes described above, calibrations for temperature and voltage variations in the timing electronics and PMTs (among other components) must be applied. These calibrations are based primarily on pre-launch testing of the temperature and voltage sensitivities of the individual components and the variations in the pixel-to-pixel performance of the photon timing system. Post-launch calibration relies on changes in the TEP-based photon times of flight, and housekeeping temperature and voltage data. Internal to each PCE is a calibration timing chain that measures how far a signal can travel during a 10 ns USO clock period. The calibration timing chain is averaged over 256 times, and telemetered once per second. Since the calibration timing chain is on the same silicon as the photon counting timing chains, this gives an in-situ measurement of any changes in the timing chain due to voltage or temperature. Analysis of reported heights for well-surveyed parts of Earth will provide an additional check on the relative consistency of photon heights among the six beams as well as the absolute height through comparison with ground-based GPS surveys (Brunt et al., 2017; Brunt et al., 2019) or high resolution airborne lidar data sets (Magruder and Brunt, 2018).

Based on pre-launch data analysis, we expect the calibrated individual photon times of flight to be accurate to ~770 picoseconds one sigma, or ~23 cm in two-way range. The primary contributors to the TOF accuracy are the transmit pulse width (~1.5 nanoseconds full width at half max) and the received photon timing uncertainty

(~400 picoseconds one sigma) owing to the characteristics of the timing electronics. Based on initial on-orbit data, ATLAS is meeting it's TOF accuracy requirements.

The precise time of flight (ph_tof) with all calibrations applied for every received photon telemetered to the ground is included in the ICESat-2 ATL02 data product in the /atlas/pcex/altimetry/strong(weak)/photons subgroup. The data product is organized by PCE card number (where pcex refers to PCE 1, 2 or 3) and several subgroups differentiate time of flight data, TEP data, and housekeeping data, among other categories.

### 3.2 Transmitter Echo Path (TEP) Photons

TEP-based photons have a much shorter time of flight (~20 ns) than photons traveling to and from the Earth (~3.3 ms). As such, in ATL02 ground processing, photons arriving ~10 to ~40 nanoseconds after a laser transmit pulse are identified as possible TEP photons. Since at times TEP photons will arrive at the same time as photons used for altimetry, possible TEP photons are included in the ATL02 data product in both the general photon cloud (aligned to the appropriate start pulse) and if present in a separate group of possible TEP photons (aligned with a much earlier start pulse) in the group /atlas/pcex/tep.

### 3.3 Other Parameters

The ATL02 data product converts raw data into engineering units for those data streams used to determine photon geolocation. Where appropriate, calibrations are applied to event timing, but for the most part, data from the LRS and spacecraft components used in the attitude or orbit determination are passed on without further modification. The ATL02 Algorithm Theoretical Basis Document (Martino et al., 2018) describes these other parameters; the full ATL02 data dictonary of the data product structure is available through NSIDC (https://nsidc.org/sites/nsidc.org/files/technical-references/ATL02-data-dictionary-v001.pdf).

## 4. The ATL03 Data Product: Global Geolocated Photons

To meet the mission science requirements (Markus et al., 2017) the individual photon times of flight from the ATL02 data product are combined with the laser pointing vectors and the position of the ICESat-2 observatory in orbit to determine the latitude, longitude and height of individual received photon events with respect to the WGS-84 ellipsoid. These geolocated photons are the main component of the ATL03 data product (Neumann et al., 2018). ATL03 also includes: a coarse discrimination between likely signal and likely background photon events; a surface classification to identify regions of land, ocean, land ice, sea ice, and inland water in the data product; several geophysical corrections to the photon heights to account for tides and atmospheric effects; metrics for the rate of background photon events; metrics for the ATLAS system-impulse response function; and a number of other ATLAS parameters which are useful to higher-level data products.

Organizationally, parameters associated with specific beams are in top-level groups in the ATL03 data product identified by ground track. For example, data from ground track 2L are found in the /gt2L/ group, and similarly for other ground tracks. Parameters common to all ground tracks (such as the spacecraft orientation parameter) are found in top-level groups such as /orbit_info/ or /ancillary_data/. The full ATL03 data dictionary is available through NSIDC (https://nsidc.org/sites/nsidc.org/files/technical-references/ATL03-data-dictionary-v001.pdf).

Both ATL02 and ATL03 data granules contain some distance of along-track data. One orbit of data is broken up into 14 granules. The granule boundaries (or granule regions) limit the granule size (nominally less than 4 GB) and where possible will simplify the formation of higher-level data products by limiting the number of granules needed to form a particular higher-level product. Granule boundaries are along lines of latitude and are depicted in Figure 7 and span about 20 degrees of latitude (or ~2200km), and are summarized in Table 2.

## 4.1 Footprint Pattern

The footprint pattern formed by the intersection of the ATLAS laser beams with the Earth's surface is shown in Figure 8, and is described in Markus et al. (2017). The ATL03 ground tracks formed by consecutive footprints are defined from left to right in the direction of travel as (ground track (GT) 1L, GT 1R, GT 2L, etc...). The mapping between beam numbering convention on ATL02 and the ground track convention of ATL03 (and higher-level products) is managed through the use of an observatory orientation parameter. The ICESat-2 observatory will be re-oriented approximately twice a year to maximize sun illumination on the solar arrays. When ATLAS is oriented in the forward orientation, the weak beams are on the left side of the beam pair, and are associated with ground tracks 1L, 2L, and 3L (Figure 8). In addition, the weak and strong beams are pitched relative to each other such that, when ATLAS is in the forward orientation, the weak beams lead the strong beams by ~2.5 km. When ATLAS is oriented in the backward orientation, the relative positions of weak and strong beams change; the strong beams are on the left side of the ground track pairs and lead the weak beams.

Over the polar regions, the ICESat-2 observatory is pointed toward the same track every 91 days, allowing seasonal height changes to be determined. Over the course of 91 days, the observatory samples 1387 such tracks, called Reference Ground Tracks (RGTs). Controlled pointing to the RGTs began in early April 2019. In the mid-latitudes, the goal of the ICESat-2 ecosystem science community is to fill in the gaps between RGTs, so the operations plan calls for a systematic off-pointing over the first two years of the mission to create as dense a mapping of canopy and ground heights as possible (see Markus et al., 2017, Figure 10).

### 4.2 Photon Geolocation and Ellipsoidal Height

To generate the geolocated height measurements of most interest to science, two additional components are needed: the pointing vectors of the ATLAS laser beams, and the position of the observatory in orbit. These two components are provided by

Precision Pointing Determination (PPD), and Precision Orbit Determination (POD). The time of flight, pointing direction and orbit position data are combined in the geolocation algorithm to provide a latitude, longitude and height for each photon telemetered by ATLAS.

The LRS is one of the most specialized devices in the PPD system. It consists of two imagers/trackers that are coaxially positioned and point in opposite directions. The LRS laser-side imager is used to determine the relative positions of the six ATLAS laser spot centroids to the four TAMS spots. These laser spot centroids help derive the pointing vector of each beam in the instrument reference frame. The LRS stellar-side imager was designed to observe stars in its field of view to determine the attitude of the satellite through the Precision Attitude Determination (PAD). The PAD uses the data streams from an onboard IMU and two spacecraft star trackers (SSTs) in an Extended Kalman Filter (EKF). The LRS stellar-side information is not currently used, owing to larger than expected sunglint on the stellar side camera, and larger than expected chromatic aberration. The EKF solution indicates the LRS orientation in the international celestial reference frame (ICRF). The final PPD product is generated by transforming the laser pointing vectors to ICRF using the knowledge of the alignment between laser-side and stellar-side. A similar approach and strategy for PPD was used for ICESat (Schutz et. al, 2008). The operational PPD algorithm was developed by the University of Texas at Austin Applied Research Laboratories and the Center for Space Research (Bae and Webb, 2016) and provides a 50 Hz time series for laser pointing unit vectors and their uncertainties for each of the ATLAS six beams to be used within the geolocation process. Although the loss of the LRS stellar-side information is unfortunate, the PPD process (and ultimate photon geolocation) is meeting mission requirements, as described below.

The algorithm to determine the position of the ICESat-2 observatory in space uses the GEODYN platform, which was developed by NASA Goddard Space Flight Center and employs detailed measurement and force modeling along with a reduced dynamic solution technique (Luthcke et al., 2003). GEODYN was used to solve for precision orbits for a variety of planetary and earth science missions, including ICESat. For ICESat-2, the POD uses the GEODYN software package along with the dual-frequency pseudorange and carrier range data from the onboard GPS receiver as well as Satellite Laser Ranging data to model the position of the observatory also in the ICRF. We expect to know the position of the observatory center of mass (CoM) to less than 3 cm radially. Early analysis of on-orbit data suggest that this is achievable.

The inputs to the photon geolocation algorithm are the round-trip photon time of flight, the transmit time of the associated laser pulse, the spacecraft position and velocity, and the spacecraft attitude- all expressed in the Earth Centered Inertial (ECI) coordinate frame. The spacecraft attitude, more specifically, is represented by the pointing vectors for each outgoing beam with appropriate corrections for velocity aberration. Additionally, the process requires determination of the laser and detector offsets with respect to the spacecraft center of mass at the transmit time of the laser pulse.

Spacecraft translational motion between the laser fire time and the photon receive time creates a disparity between the photon path to the Earth and the photon path back to the observatory. The rigorous geolocation and altimeter measurement models perform the light time solution to accommodate the travel time disparity and apply the necessary spacecraft velocity aberration correction for the purpose of precision in the direct altimetry. However, for the purposes of geolocation only, ICESat-2 uses a simple and sub-millimeter accurate approximation that avoids the need for the light time solution modeling. This approximation effectively accounts for the mean motion of the spacecraft over the course of the photon's flight time and allows us to solve for the photon bounce point in ECI.

Atmospheric refraction plays a critical role in the bounce point determination but is difficult to determine without the coordinates of the bounce point. To mitigate this issue an approximate bounce point is calculated using the spacecraft pointing vector, the laser pointing vector, and the two-way range. This gives an initial atmospheric refraction correction which is used to determine the photon receive time, and the position of the spacecraft center of mass at the photon receive time.

Once time of flight, position and pointing parameters are determined the bounce point is a simple vector calculation to produce the location in ECI. The ECI position is then converted to earth centered fixed (ECF) coordinates by accounting for the precession, nutation, the spin, and polar motion of the Earth. And lastly, the ground bounce point is transformed into the international terrestrial reference frame (ITRF; Petit and Luzum 2010) as latitude, longitude, and elevation with respect to the WGS-84 (G1150) ellipsoid based on ITRF 2014 ($a_e$ = 6378137 m, 1/f = 298.257223563). At this point in the geolocation determination, we refine the refraction correction and tropospheric delay parameters, and re-geolocate the photon following the procedure above.

Instead of precisely geolocating every received photon, which would be computationally expensive, the process geolocates a single photon in every ~20m along-track segment on the surface. These are referred to as the reference photons. The reference photon is chosen from among the high-confidence likely signal photons (should any be present). If no high-confidence photons are found, we use either a medium- or low-confidence photon. Failing that, we use a likely background photon as the reference photon. Finally, static and time varying instrument pointing, ranging and timing biases are applied to correct for on-orbit instrument variations. These biases are estimated from the rigorous direct altimetry range residual analysis using special spacecraft conical calibration maneuvers and from dynamic crossovers (Luthcke et al. 2000 and 2005).

A detailed geolocation budget based on all subsystem performance requirements and current best estimates of ranging, timing, positioning and pointing has been established to track the quality of the geolocation solution pre-launch. Once on-orbit these estimates evolve to include post-calibration assessments for understanding of the performance through full system development and testing. The mission requirement for single photon horizontal geolocation is 6.5 m one sigma. The best estimate of this accuracy pre-launch is 4.9 m one sigma, but finalizing the on-orbit value will require several months of calibration and validation data sampling over the full sun-orbit geometry.

Estimating the errors in the resulting photon latitude, longitude, and ellipsoidal height are described thoroughly by Luthcke et al. (2018). These uncertainties are largely determined by the accuracy of the primary input data- spacecraft attitude, position and the photon time of flight. We assume the position uncertainties, represented in the ECI coordinate frame and separated into radial, along-track and cross-track components, have zero mean. The ranging errors are decomposed into contributions from time-of-flight measurement, instrument bias estimate and errors attributed to atmospheric path delay. The attitude or pointing errors are determined within the precision pointing determination algorithm (Bae et. al, 2016), also expressed in the ECI frame. The contributions from each error source are combined and represented to the user in the ECF coordinate system and subsequently the geodetic frame. The ATL03 data product reports the uncertainty for latitude, longitude and elevation on each reference photon.

Although any given transmitted laser pulse may have between 0 and ~12 returned signal photons in addition to background photons, each received photon is aligned with a specific laser transmit pulse. As such, the along-track time for each received photon (the absolute event time) associated with a given transmit laser pulse is the same and corresponds to the laser transmit time. Additional data is available on the product to determine the ground bounce time of the photons, if desired. The latitude, longitude and height of each photon is unique, due to the non-nadir pointing angle of any of the six ATLAS beams and the topography of the Earth's surface.

The latitude, longitude and height (along with the associated uncertainties) of each telemetered photon event (lat_ph, lon_ph, h_ph) are provided on the ICESat-2 ATL03 data product, grouped according to ground track. Data at the photon rate (e.g. latitude, longitude, height) are in the /gtx/heights group for each ground track. Data at the geolocation segment rate (nominally ~20m) are in the /gtx/geolocation group for each ground track.

### 4.3 Surface Classification Masks

ATL03 includes a set of surface classification masks which tessellates the Earth into land, ocean, sea ice, land ice, and inland water areas. These classification masks overlap by ~20 km and ensure that surface-specific higher-level geophysical data products are provided with the appropriate photons from ATL03. The surface classification masks are not exclusive; several areas on Earth have more than one classification (e.g. land and ocean) due to overlap between surface types (for example along coasts) or due to non-unique definitions (land and land ice). In those regions that have multiple classification a higher-level geophysical product will be produced for each representative class. Higher-level data products further trim the set of photons that are used in those products (e.g. the higher-level sea ice data products exclude areas of open ocean).

## 4.4 Photon Classification Algorithm

The telemetered photon events contain both signal and background photon events. ATL03 processing uses an algorithm to provide an initial discrimination between signal and background photon events (Neumann et al., 2018). The goal of this algorithm is to identify all the signal photon events while classifying as few as possible of the background photon events erroneously as signal. The algorithm generates along-track histograms, identifies likely signal photon events by finding regions where the photon event rate is significantly larger than the background photon event rate, and uses surface-specific parameter choices to optimize performance over land, ocean, sea ice, land ice and inland water.

The initial task in the overall signal finding is to determine the background photon event rate. The vertical span of telemetered photon events is limited (30 m to 3000 m), so the downlinked photon data is not optimal for calculating a robust background count rate. However, for atmospheric research (Palm, et al. 2018), ICESat-2 telemeters histograms of the sums of all photons over four hundred laser transmit pulses (0.04 s; ~280 m along-track) in 30 m vertical bins for ~14 km in height. These histograms, referred to as atmospheric histograms, include photons reflected off atmospheric layers, background photons and surface-reflected photons. After removing the relatively few bins that may contain signal photon events from these atmospheric histograms, the algorithm uses the remaining bins to estimate the background photon event rate. Nominally, the atmospheric histograms will only be downlinked for the strong beams. The weak beam background photon event rate is calculated from the strong beam atmospheric histogram after consideration of the fore/aft offset between the weak and strong beams. When an atmospheric histogram is not available, the photon cloud itself is used to determine the background count rate. The background photon rate used in further analysis is reported on the ATL03 data product.

The algorithm uses the resulting background rate to determine a threshold to identify likely signal photons. It then generates a histogram of photon ellipsoidal heights and distinguishes signal photons from background photons based on the signal threshold. If the initial choice of along-track and vertical bin sizes does not find signal, the along-track integration and/or vertical bin heights are increased until either signal is identified or limits on the bin size are reached. Depending on the signal-to-noise ratio, photons are classified as high-confidence signal ($SNR \geq 100$), medium-confidence signal ($100 > SNR \geq 40$), low confidence signal ($40 > SNR \geq 3$), or likely background ($SNR < 3$). Data from each beam and for each potential surface type are considered independently for the ellipsoidal histogramming procedure (except for the background rate calculation).

Over sloping surfaces, the surface photons can be spread over a range of heights so that they are not readily found with ellipsoidal histogramming. To identify these, a histogram is generated relative to an angled surface, where the angle is either defined by the surrounding signal photons identified through ellipsoidal histograms (if extant) or by testing a range of plausible surface slope angles. This procedure is referred to as slant histogramming. An example of the photon classification algorithm output is shown in Figure 9 for a strong beam.

Since the signal-to-noise ratio is larger for the strong beam than the weak beam, the strong beam should provide a better definition of the surface than the weak beam. The ground tracks of a strong and weak beam pair are parallel to each other, and separated by ~90 m, so the slopes of the resultant surface profiles should be similar in most cases. Therefore, for the weak beam of each pair, the algorithm uses the surface profile found in the strong beam to guide slant histogramming of the adjacent weak beam.

In general, each higher-level data product requires ATL03 to identify likely signal photon events within +/- 10 m of the surface. Since the ATL03 algorithm uses histograms, the vertical resolution at which signal photons are selected is directly proportional to the histogram bin size. All photons in a given bin are either classified as signal or background events. One of the design requirements of the algorithm is to classify photons at the finest resolution possible and use the smallest possible bin size. When the vertical span of likely signal photons is less than ~20 m, we flag additional photons to ensure that higher level products always consider a vertical column of photons spanning at least 20 m.

On the ATL03 product, the photon classification is given by the signal_conf_ph parameter in the /gtx/heights group for each beam. As noted above, the algorithm uses surface-specific choices to classify photons slightly differently depending on the surface type. As such, the signal_conf_ph array has five values for each photon (or is dimensioned as 5 x N, where N is the number of photons), corresponding to the five surface types (land, ocean, sea ice, land ice, inland water). Specific values are 4 (high confidence signal), 3 (medium confidence signal), 2 (low confidence signal), 1 (likely background but flagged to insure at least 20 m of photons are flagged), 0 (likely background), -1 (surface type not present), and -2 (likely TEP photons). The parameters used to classify photons from a given ATL03 data granule are also provided on that data granule.

### 4.5 Geophysical Corrections

To readily compare ATL03 signal photon heights collected from the same location at different times and to facilitate comparisons with other data sources, photon heights are corrected for several geophysical phenomena. These corrections are globally defined (taking a value of zero where appropriate) and are designed to be easily removed by an end user to allow application of a regional model that better captures local variation.

The set of geophysical corrections applied on the ATL03 data product include solid earth tides, ocean loading, solid earth pole tide, ocean pole tide, and the wet and dry atmospheric delays. Additional reference parameters on the ATL03 data product include the EGM2008 geoid, the ocean tide as given by the GOT4.8 model (Ray, 1999, updated), and the MOG2D dynamic atmospheric correction / inverted barometer as calculated by AVISO (http://www.aviso.oceanobs.com/en/data/products/auxiliary-products/atmospheric-corrections.html). The full set of corrections is described in Markus et al. (2017) and more thoroughly in Neumann et al. (2018). The resulting geophysically-corrected photon heights ($H_{GC}$) in the ATL03 data product are therefore:

$$H_{GC} = H_P - H_{OPT} - H_{OL} - H_{SEPT} - H_{SET} - H_{TCA}$$

where $H_p$ is the photon height about the WGS-84 ellipsoid, $H_{OPT}$ is the height of the ocean pole tide, $H_{OL}$ is the height of the ocean load tide, $H_{SEPT}$ is the height of the solid earth pole tide, $H_{SET}$ is the height of the solid earth tide, and $H_{TCA}$ is the height of the total column atmospheric delay correction. All values are beam-specific, are calculated at the geolocation segment rate (~20 m), and are found in the /gtx/geophys_corr group on ATL03. End users who prefer to remove one or more of these corrections can do so by adding the relevant terms (e.g. $H_{OL}$) to $H_{GC}$.

### 4.6 System Impulse Response Function

To determine high-quality geolocated Earth surface heights, it is necessary to refine the coarse signal finding provided on the ATL03 data product. Higher-level algorithms use strategies specific to each surface type, which take into consideration the science questions of greatest interest and the geophysical phenomena specific to each surface type. For example, the interior of the ice sheets has a large surface reflectivity at 532 nm, allowing a relatively short length-scale product to be generated (~40 m along track; Smith et al., this issue), while over the ocean the small surface reflectivity requires aggregating likely signal photon events over longer distances (~7000 m, or one second of along-track data). Higher-level data products use the system impulse response function of ATLAS in order to improve surface height estimates (e.g. through deconvolution).

As noted above, the TEP provides a means to monitor both the on-orbit range bias change and the average system impulse response function for the two strong beams. Each ATL03 data granule includes the most recent accepted measurement set of TEP photons and provides a histogram of their transmit times in the /atlas_impulse_response group.

Given the low rate at which TEP photon events are generated (approximately 1 photon per 20 ATLAS laser transmit pulses), a significant number of TEP photons must be aggregated to adequately act as a proxy for the average ATLAS impulse response function. ATL03 aggregates at least 2000 possible TEP photons (identified in the ATL02 data product) into a single estimate of the ATLAS system impulse response function. These photons are histogrammed into 50 ps wide bins, the background rate is determined (after excluding the region with the TEP return), and subtracted from each bin. The resulting histogram is then scaled to unit area (Figure 10). It is important to note that the resulting ATLAS system impulse response function estimate is an average over the duration that likely TEP photons have been aggregated over (~seconds to minutes), and short timescale shot-to-shot variation is not captured. However, higher-level data products (e.g. Smith et al., this issue) aggregate data from many consecutive shots negating the need for shot-based impulse-response function.

During nominal operation, likely TEP photon events are telemetered along with the likely surface echoes approximately twice per orbit. Given that there are 14 granules per orbit (see Figure 7), this means that for any particular ATL03 data granule, the TEP data may come from a different part of the orbit. ATL03 provides the TEP data collected most recently in time with respect to a prior or subsequent ATL03 data granule.

## 5. ATL03 Data Validation

We developed a plan to validate the geolocations of the received photon events reported on ATL03. The validation plan includes: a statistical analysis of the ICESat-2 ground-track crossovers; comparisons of ATL03 photon heights with airborne datasets; comparisons of ATL03 photon heights with ground-based datasets; and comparisons of ATL03 photon latitude, longitude and height with known locations of corner cube retroreflectors (CCRs). These assessments are made on data posted at the photon rate (in the /heights group for each ground track).

A crossover analysis (Luthcke et al., 2005) will be used to assess the internal consistency of ATL03 ellipsoidal heights. These analyses compare heights of data from both ascending and descending ICESat-2 ground tracks, specifically where these tracks intersect, or cross one another, within a given 24-hour period. Further, we limit these analyses to ice sheet interior regions (Figure 11), where the surface is flat (slope << 1°) and errors associated with geolocation are minimized. Since these analyses are restricted to ATL03 data and do not include ground-truth data from an outside source, this is an assessment of repeatability (or ground-measurement relative accuracy).

Direct comparison of ATL03 ellipsoidal heights with ground truth will be used to assess the absolute bias, or accuracy of the data. There are two ground-based surveys on ice sheets designed to validate ATL03 photon heights. The first is a 7 km along-track traverse near Summit Station, Greenland (Brunt et al., 2017). While this traverse does not represent a long length-scale of data, this survey has been conducted monthly since August 2006 (Siegfried et al., 2011) and represents the longest and densest time series of height measurements in the center of an ice sheet. This traverse will continue through the three-year nominal mission duration.

A second ground-based survey, the 88S Traverse (Brunt et al., 2019), will be used for ATL03 ellipsoidal height validation. The traverse intersects the data-dense region of ICESat-2 ground tracks, near the 88S line of latitude approximately 224 km north of South Pole Station, Antarctica. The 300 km traverse is a long length scale of data and intersects approximately 277 ICESat-2 ground tracks. The first two traverses were conducted during the 2017-18 and 2018-19 Antarctic field seasons; two additional annual traverses will be conducted during the nominal mission duration.

Data from the Summit and 88S traverses have been used to provide error assessments for three different NASA Operation IceBridge airborne laser altimeters (Brunt et al., 2017; Brunt et al., 2019). Knowledge of the airborne instrument error (absolute height accuracy and surface-measurement precision) enables height data from these instruments to be used for direct comparisons with ATL03 ellipsoidal heights; further these comparisons can be made on longer length-scales than what is reasonable for a ground-based campaign (>300 km). Thus, many of the flights associated with the Operation IceBridge campaigns have been designed to meet the mission goals of the airborne campaign and to simultaneously provide large datasets for ICESat-2 validation, including flights along the Summit and 88S ground-based traverses. Operation IceBridge data was used to assess the sea ice freeboard retrievals from CryoSat-2 (Yi et al., 2018) and a similar approach will be used to assess ICESat-2 sea ice freeboard estimates.

The accuracy of ATL03's photon geolocation will be assessed by direct comparison of photons reflected from corner cube retroreflectors (CCRs; Magruder and Brunt, 2018) with independently measured locations. Whereas the previous validation strategies only addressed ellipsoidal height, a CCR analysis also includes latitude and longitude evaluation. A series of arrays of CCRs have been deployed along the 88S Traverse and at White Sands Missile Range, NM (Magruder et al., 2007) (Figure 12). The latitude and longitude of the CCRs are known based on precise GPS measurements of the location of the staffs holding the CCR, and the relative height of the CCR above the surface is also measured. The size of the glass prisms has been optimized for the ATLAS wavelength and velocity of the ICESat-2 observatory.

## 6. Summary

The Ice, Cloud and Land Elevation Satellite-2 (ICESat-2) observatory carries a state-of-the-art laser ranging instrument (ATLAS). The ATLAS laser generates a single 532 nm laser pulse that is split into six beams from an orbit 500 km above Earth's surface and records the transmit time of these laser pulses. The ATLAS receiver system records the arrival time of the returning laser light by single-photon sensitive detectors. The precise photon times of flight are determined from these transmit and receive times and are provided in the ATL02 data product, among other data. The ATL03 data product combines the photon time of flight with observatory attitude and position data to determine the geodetic location (latitude, longitude and height) for each photon in the ATL02 data product. The quality of the ATL03 geolocation solutions is validated through comparison with independent measurement from aircraft and ground surveys. The ATL03 product is the primary input to higher-level products that enable science discovery across many scientific fields, including the study of glaciers and ice sheets, sea ice, terrestrial ecology, oceanography, atmospheric science, and inland water hydrology.

## 7. Acknowledgements

We express our gratitude to the hundreds of people at NASA Goddard Space Flight

Center and contracting partners (notably Northrop Grumman Innovation Systems) that conceived, designed, and created ICESat-2 Mission, the ICESat-2 Observatory, and the ATLAS instrument. We thank Dr. Helen Fricker, Dr. Tom Armitage, and two anonymous reviewers for comments that substantially improved this manuscript. Thanks to Aimée Gibbons for assistance with several figures.

## Figure Captions

**Figure 1.** The ICESat-2 observatory. Laser light is transmitted and returns to the nadir-looking face of the observatory (upper); the star trackers and GPS antennas are on the zenith-looking face (lower).

**Figure 2.** The major components of the ATLAS transmitter. Components discussed in the text include the two laser transmitters, the Laser Sampling Assembly, the Beam Shaping Optics, Beam Steering Mechanism, and the Diffractive Optical Element. Arrows denote the optical path through the transmitter; arrow width is a proxy for relative energy.

**Figure 3.** Schematic of the ATLAS receiver. Major components described in the text are the Telescope, Optical Fibers, Optical Filters, and Detector Modules. Green arrows denote the optical path; red arrows denote communication and commanding from the ATLAS avionics system; dark green arrows denote the Telescope Alignment and Monitoring System (TAMS) path, which is described in Section 2.1.4 and shown in Figure 5.

**Figure 4.** Design of the ATLAS multi-pixel photo-multiplier tube configuration for the three weak and three strong beams. Each strong beam uses the 16 pixels (numbered 1 – 16) individually to generate 16 independent electrical outputs, while each weak beam combines four pixels together to effectively create a four-pixel

detector (pixels PA, PB, PC, and PD) to generate four independent electrical outputs.

**Figure 5.** Primary components of the ATLAS Alignment Monitoring and Control System (AMCS). The AMCS provides a means to keep the transmitted laser light from the beam steering mechanism (BSM) aligned with the receiver fields of view. Bright green arrows indicate the pathway of 532 nm green light; red arrows indicate power and commanding from the avionics system; dark green arrows indicate the pathway of light from the Telescope Alignment and Monitoring System (TAMS) light source. A portion of the transmitted beams and TAMS beams are routed to the Laser Reference System (LRS) using lateral transmit retroreflectors (LTRs).

**Figure 6.** The ATLAS start pulse is timed at four places along the transmitted pulse profile. Each PCE card records the time of the leading lower crossing time, as well as one other crossing time. By recording a common event across all cards, the times of events can be aligned.

**Figure 7.** ATL03 regions. Region boundaries are used as boundaries between ATL02 data granules. Each complete orbit is broken into 14 distinct granules as indicated.

**Figure 8.** The ATLAS beam pattern on the ground changes depending on the orientation of the ICESat-2 observatory. The pattern on top corresponds to traveling in the forward (+x) orientation, while the pattern on the bottom corresponds to

traveling in the backward (-x) orientation. The numbers indicate the corresponding ATLAS beam, while the L/R mapping are used on the ATL03 and higher-level data products. The two strong beams with the TEP are ATLAS beams 1 and 3. Derived from Markus et al. (2017), Figure 2.

**Figure 9.** Top: Signal and background photons collected by ATLAS over Greenland, 9 November 2018. Bottom: Resulting classification of high-confidence (blue), medium-confidence (red), and low-confidence (green) likely signal photons. Inset shows detail of photon cloud over water surface.

**Figure 10.** A normalized histogram of transmitter echo path (TEP) photons. The x-axis is the TEP photon time of flight (TOF) in nanoseconds, and y-axis is normalized counts. Histogram bins are 50 ps wide, and the histogram is composed of TEP photons from 3,308,000 unique laser fires, or about 300,000 TEP photons.

**Figure 11.** Masks used for ICESat-2 crossover analysis. The red and green polygons represent the regions used for the crossover analysis. The red polygon on the East Antarctic Ice Sheet was chosen based on a height mask (2400 m.a.s.l.); the green polygon was added to incorporate some data from the West Antarctic Ice Sheet. The yellow points represent the crossovers that occurred during a single day (there are generally around 100 per day).

**Figure 12.** CCR deployment. Left: a CCR being deployed along the 88S Traverse,

with the precise latitude and longitude being surveyed with a GPS. Right: a CCR mounted on the top of a bamboo pole along the 88S Traverse.

**References:**

Abshire, J.B., Sun, X., Riris, H., Sirota, J.M., McGarry, J.F., Palm, S., Yi, D., Liiva, P., 2005. Geoscience Laser Altimeter System (GLAS) on the ICESat Mission: On-orbit measurement performance. Geophys. Res. Lett, 32(L21S02), doi: 10.1029/2005GL024028.

Bae, S. and Webb, C.E., 2017. Precision Attitude Determination with an extended Kalman filter to measure ice sheet elevation. Journal of Guidance, Control, and Dynamics, 40(9), 2335-2340, doi:10.2514/1.G002715.

Blarre L., Ouaknine, J., Oddo-Marcel, L., Martinez, P.E., 2006. High accuracy Sodern Star Trackers: Recent improvements proposed on SED36 and HYDRA Star Trackers, AIAA Guidance, Navigation, and Control Conference, doi:10.2514/6.2006-6046.

Brunt, K.M., Hawley, R., Lutz, E., Studinger, M., Sonntag, J., Hofton, M., Andrews, L., and Neumann, T., 2017. Assessment of NASA airborne laser altimetry data using ground-based GPS data near Summit Station, Greenland, The Cryosphere, 11, 681–692, doi:10.5194/tc-11-681-2017.

Brunt, K.M., Neumann, T., and Larsen, C.F., 2019. Assessment of altimetry using ground-based GPS data from the 88S Traverse, Antarctica, in support of ICESat-2, The Cryosphere, 13, 579-590, doi:10.5194/tc-2018-160.

Degnan, J.J., 2002. Photon-counting multikilohertz microlaser altimeters for airborne and spaceborne topographic measurements, Journal of Geodynamics, 34, 503-549.

Fricker, H. A, Borsa, A. Minster, B., Carajabal, C., Quinn, K., Bills, B., 2005. Assessment of ICESat performance at the Salar de Uyuni, Bolivia. Geophys. Res. Lett., 32(L21S06), doi:10.1029/2005GL023423.

Kwok, R., Cunningham, G. F., Hoffmann, J., Markus, T., 2016. Testing the ice-water discrimination and freeboard retrieval algorithms for the ICESat-2 mission, Remote Sensing of the Environment, 183, 13-25. 10.1016/j.rse.2016.05.011.

Leigh, H.W., Magruder, L.A., Carabajal, C.C., Saba, J.L., McGarry, J.F., 2014. Development of onboard digital elevation and relief databases for ICESat-2, IEEE Transactions on Geoscience and Remote Sensing, 53(4), 10.1109/TGRS.2014.2352277.

Luthcke, S.B., Rowlands, D.D., McCarthy, J.J., Stoneking, E., Pavlis, D.E., 2000. Spaceborne laser altimeter pointing bias calibration from range residual analysis, Journal of Spacecraft and Rockets, 37(3), 374-384.

Luthcke, S.B., Carabajal, C.C., Rowlands, D.D. 2002. Enhanced geolocation of spaceborne laser altimeter surface returns: Parameter calibration from the simultaneous reduction of altimeter range and navigation tracking data. Journal of Geodynamics, 34(3-4), 447-475.

Luthcke, S. B., Zelensky, N.P. Rowlands, D.D., Lemoine, F.G., Williams, T.A., 2003. The 1-centimeter orbit: JASON-1 Precise Orbit Determination using GPS, SLR, DORIS, and altimeter data. Marine Geodesy, 26(3-4), doi:10.1080/714044529.

Luthcke, S. B., Rowlands, D.D., Williams, T.A., Sirota, M., 2005. Calibration and reduction of ICESat geolocation errors and the impact on ice sheet elevation change detection. Geophysical Research Letters, 32(21). doi:10.1029/2005GL023689.

Luthcke, S.B., Pennington, T., Rebold, T., Thomas, T., 2018. Ice, Cloud, and land Elevation Satellite (ICESat-2) Project Algorithm Theoretical Basis Document for the ICESat-2 Receive Photon Geolocation.

McGill M., Markus, T., Scott, V.S., Neumann, T., 2013. The multiple altimeter beam experimental lidar (MABEL): An airborne simulator for the ICESat-2 mission. J. Atmos. Ocean. Technol. 30(2), 345-352, doi:10.1175/JTECH-D-12.00076.1.

Magruder, L.A., Webb, C.E., Urban, T.J., Silverberg, E.C., Schutz, B.E., 2007. ICESat altimetry data product verification at White Sands Space Harbor. IEEE Transactions on Geoscience and Remote Sensing, 45(1), 147-155, doi:/10.1109/TGRS.2006.885070.

Magruder, L.A., Brunt, K.M., 2018. Performance analysis of airborne photon-counting lidar data in preparation of ICESat-2, IEEE Transactions on Geoscience and Remote Sensing, 56(5), 2911–2918, doi:10.1109/TGRS.2017.2786659.

Markus, T., Neumann, T., Martino, A., Abdalati, W., Brunt, K., Csatho, B., Farrell, S., Fricker, H., Gardner, A., Harding, D., Jasinski, M., Kwok, R., Magruder, L., Lubin, D., Luthcke, S., Morison, J., Nelson, R., Neuenschwander, A., Palm, S., Popescu, S., Shum, C.K., Schutz, B.E., Smith, B., Yang, Y., Zwally, H.J., 2017. The Ice, Cloud and land Elevation Satellite-2 (ICESat-2): Science requirements, concept, and implementation. Remote Sensing of the Environment, 190, 260-273, doi: 10.1016/j.rse.2016.12.029.

Martino, A.J., Bock, M.R., Jones R.L. III, Neumann, T.A., Hancock, D.W., Dabney, P.W., Webb, C.E., 2018. Ice Cloud and Land Elevation Satellite – 2 Project Algorithm Theoretical Basis Document for ATL02 (Level-1B) data product processing. https://icesat-2.gsfc.nasa.gov/science/data-products.

Montenbruck, O., Hackel, S., Jäggi, A., 2017. Precise orbit determination of the Sentinel-3A altimetry satellite using ambiguity-fixed GPS carrier phase observations. Journal of Geodesy, 92(7), 711-726, doi:10.1007/s00190-017-1090-2.

National Research Council, Earth Science and Applications from Space: National Imperatives for the Next Decade and Beyond. Washington, D.C.: The National Academies Press. https://doi.og/10.17226/11820.

Neuenschwander, A., Pitts, K., 2018. The ATL08 Land and Vegetation Product for the ICESat-2 Mission. Remote Sensing of Environment, Remote Sensing of Environment, 221, 247-259, https://doi.org/10.1016/j.rse.2018.11.005.

Neumann, T.A., Brenner, A.C., Hancock, D.W., Karbeck, K., Luthcke, S., Robbins, J., Saba, J., Gibbons, A., 2018. Ice, Cloud, and Land Elevation Satellite-2 Project Algorithm Theoretical Basis Document for Global Geolocated Photons (ATL03). https://icesat-2.gsfc.nasa.gov/science/data-products.

Palm, S., Yang, Y, Herzfeld, U., 2018. ICESat-2 Algorithm Theoretical Basis Document for the Atmosphere, Part 1: Level 2 and 3 Data Products. https://icesat-2.gsfc.nasa.gov/science/data-products.

Pearlman, M.R., Degnan, J.J., Bosworth, J., 2002. The international laser ranging service, Advances in Space Research, 30(2), 135-143, doi: 10.1016/S0273-1177(02)00277-6.

Petit, G., Luzum, B., 2010. IERS Conventions (2010), IERS Technical Note No. 36, International Earth Rotation and Reference System Service.

Ray, R.D., 1999. A global ocean tide model from Topex/Poseidon altimetry: GOT99.2, NASA Tech Memo 209478.

Sawruk, N.W., Burns, P.M., Edwards, R.E., Wysocki, T., VanTuijl, A., Litvinovitch, V., Sullivan, E., Hovis, F.E., 2015. ICESat-2 laser technology readiness level evolution, Solid State Lasers CCIV: Technology and Devices, SPIE 9342, doi: 10.1117/12.2080531.

Schutz, B.E., Zwally, H.J., Shuman, C.A., Hancock, D., DiMarzio, J.P., 2008. Overview of the ICESat mission, Geophys. Res. Lett., 32(21), doi:10. 1029/2005GL024009.

Schutz, B.E., Bae, S., Smith, N., Sirota, M., 2008. Precision orbit and attitude determination for ICESat, Advances in Astronautical Sciences.

Sharma, A., Walker, J.G., 1992. Paralyzable and nonparalyzable deadtime analysis in spatial photon counting. Review of Scientific Instruments 63 (5784), doi:10.1063/1.1143364.

Siegfried, M.R., Hawley, R.L., Burkhart, J.F., 2011, High-resolution ground-based GPS measurements show intercampaign bias in ICESat elevation data near Summit, Greenland. IEEE Transactions on Geoscience and Remote Sensing, 49(9), 3393-3400.

Smith, B.E., Fricker, H.A., Holschuh, N., Gardner, A.S., Adusumilli, S., Brunt, K.M., Bsatho, B., Harbeck, K., Huth, A., Neumann, T.A., Nilsson, J., Siegfried, M.R., this issue, Land ice height-retreival algorithms for NASA's ICESat-2 photon-counting laser altimeter. Remote Sensing of the Environment, in press.

Sun, X., Abshire, J.B., Borsa, A.A., Fricker, H.A., Yi, D., Dimarzio, J.P., Neumann, G.A., 2017. ICESat/GLAS altimetry measurements: received signal dynamic range and saturation correction. IEEE Transactions on Geoscience and Remote Sensing, 55(10), 5440-5454.

Webb, C., Zwally, H., Abdalati, W., 2012. The Ice, Cloud, and land Elevation Satellite (ICESat) Summary Mission Timeline and Performance Relative to Pre-Launch Mission Success Criteria. NASA Technical Report, NASA/TM-2013-217512.

Williamson, J.A., Kendall-Tobias, M.W., Buhl, M., Seibert, M., 1988. Statistical evaluation of dead time effects and pulse pileup in fast photon counting. Introduction of the sequential model. Analytical Chemistry, 60(20), 2198-2203, doi:10.1021/ac00171a007.

Yi, D., Kurtz, N., Harbeck, J., Kwok, R., Hendricks, S., Ricker, R., 2018. Comparing coincident elevation and freeboard from IceBridge and five different CryoSat-2 retrackers. IEEE Transactions on Geoscience and Remote Sensing, 99, doi:10.1109/TGRS.2018.2865257.

Zwally, H.J., Schutz, B., Abdalati, W., Abshire, J., Bentley, C., Brenner, A., Bufton, J., Dezio, J., Hancock, D., Harding, D., Herring, T., Minster, B., Quinn, K., Palm, S., Spinhirne, J., Thomas, R., 2002. ICESat's laser measurements of polar ice, atmosphere, ocean, and land. Journal of Geodynamics, 34, 405-445.

| | |
|---|---|
| **Transmitter** | |
| Pulse repetition frequency (kHz) | 10 |
| wavelength (nanometers) | 532.272 ± 0.15 |
| footprint diameter (m; microradians) | <17.4; <35 at 85% encircled energy |
| pulsewidth (nanoseconds, FWHM) | < 1.5 |
| pulse energy (millijoules) | 0.2 to 1.2 |
| optical throughput efficiency | 73% |
| number of beams | 6 |
| beam energy ratio (strong:weak) | 4:1 |
| beam energy per pulse (strong, weak, microjoules) | 175 ±17, 45 ±5 |
| | |
| **Receiver** | |
| telescope diameter (m) | 0.8 |
| receiver field of view (m, microradians) | 45, 83.3 |
| coarse filter bandbass (picometers) | 200 |
| optical filter bandpass (picometers) | 30 |
| optical throughput efficiency | 42% |
| detector efficiency | 15% |

**Table 1.** Major characteristics of the ATLAS transmitter and receiver.

| Region Number | Ascending / descending | Beginning latitude | Ending latitude |
|---|---|---|---|
| 1 | Ascending | equator | 27 N |
| 2 | Ascending | 27 N | 59.5 N |
| 3 | Ascending | 59.5 N | 80 N |
| 4 | Ascending / Descending | 80 N | 80 N |
| 5 | Descending | 80 N | 59.5 N |
| 6 | Descending | 59.5 N | 27 N |
| 7 | Descending | 27 N | equator |
| 8 | Descending | Equator | 27 S |
| 9 | Descending | 27 S | 50 S |
| 10 | Descending | 50 S | 79 S |
| 11 | Descending / Ascending | 79 S | 79 S |
| 12 | Ascending | 79 S | 50 S |
| 13 | Ascending | 50 S | 27 S |
| 14 | Ascending | 27 S | Equator |

**Table 2.** Geographic boundaries of ATL02 and ATL03 granules.

| | |
|---|---|
| ATLAS | Advanced Topographic Laser Altimeter System |
| AMCS | Alignment Monitoring and Control System |
| ATL02 | ICESat-2 Science Unit Converted Telemetry Level 1B Data Product |
| ATL03 | ICESat-2 Global Geolocation Photon Level 2A Data Product |
| BSM | Beam Steering Mechanism |
| CCR | Corner Cube Retroreflector |
| CoM | Observatory Center of Mass |
| DOE | Diffractive Optical Element |
| ECF | Earth Centered, Fixed |
| ECI | Earth Centered, Inertial |
| EKF | Extended Kalman Filter |
| ESA | European Space Agency |
| GLAS | Geosciences Laser Altimeter System |
| ICESat | Ice Cloud and Land Elevation Satellite |
| ICESat-2 | Ice Cloud and Land Elevation Satellite - 2 |
| ICRF | International Celestial Reference Frame |
| IERS | International Earth Rotation and Reference System |
| IMSC | Instrument Mounted Spacecraft Components |
| IMU | Inertial Measurement Unit |
| ITRF | International Terrestrial Reference Frame |
| LRS | Laser Reference System |
| LTR | Lateral Transfer Retroreflector |
| MABEL | Multiple Altimeter Beam Experimental Lidar |
| MRF | Master Reference Frame |
| PAD | Precision Attitude Determination |
| PCE | Photon-Counting Electronics |
| PMT | Photomultiplier Tube |
| POD | Precision Orbit Determination |
| PPD | Precision Pointing Determination |
| PRF | Pulse Repetition Frequency |
| RGT | Reference Ground Track |
| SPD | Start Pulse Detector |
| SSIRU | Scalable Space Inertial Reference System |
| SST | Spacecraft Star Tracker |
| TAMS | Telescope Alignment and Monitoring System |
| TEP | Transmitter Echo Path |
| TOF | Time of Flight |

| | |
|---|---|
| USO | Ultra Stable Oscillator |
| WGS | World Geodetic System |
| WTOM/WTEM | Wavelength Tracking Optical / Electronics Module |
| ZRP | Zero Range Point |

**Table 3.** Glossary of acronyms used in text.

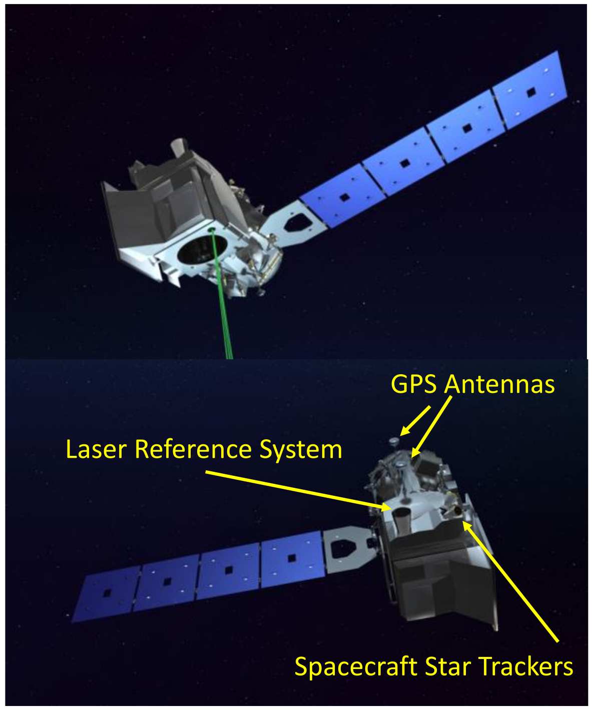


**Figure 1.** The ICESat-2 observatory. Laser light is transmitted and returns to the nadir-looking face of the observatory (upper); the star trackers and GPS antennas are on the zenith-looking face (lower).

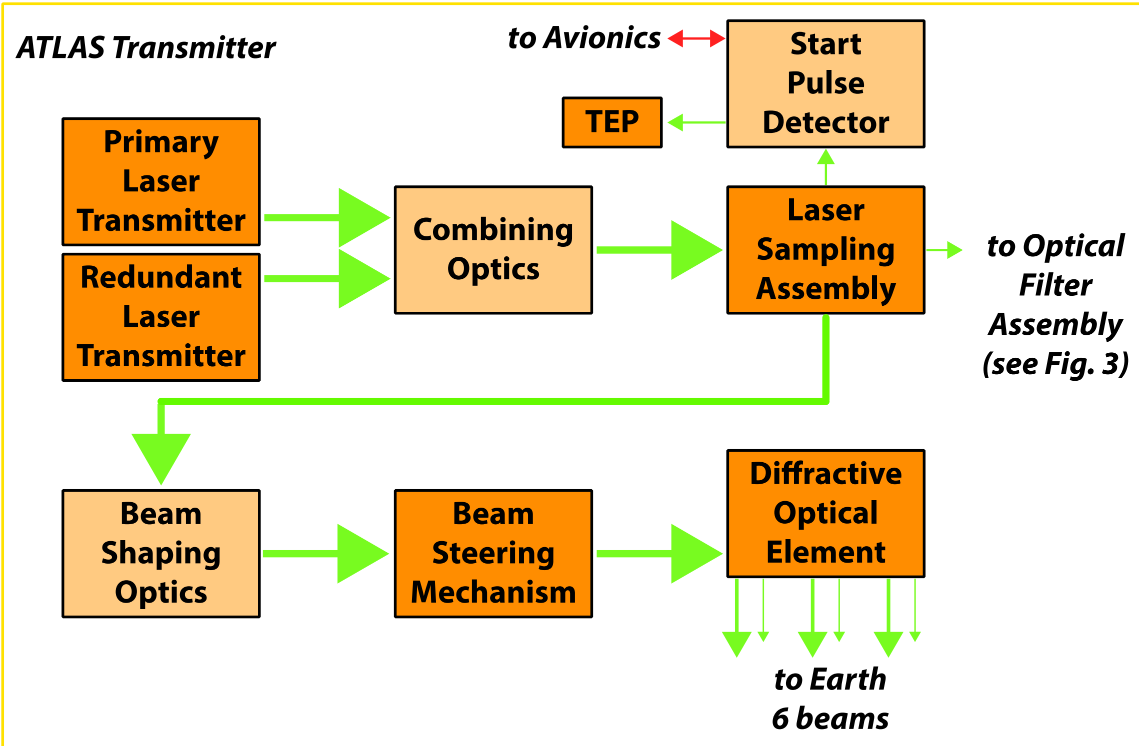


**Figure 2.** The major components of the ATLAS transmitter. Components discussed in the text include the two laser transmitters, the Laser Sampling Assembly, the Beam Shaping Optics, Beam Steering Mechanism, and the Diffractive Optical Element. Arrows denote the optical path through the transmitter; arrow width is a proxy for relative energy.

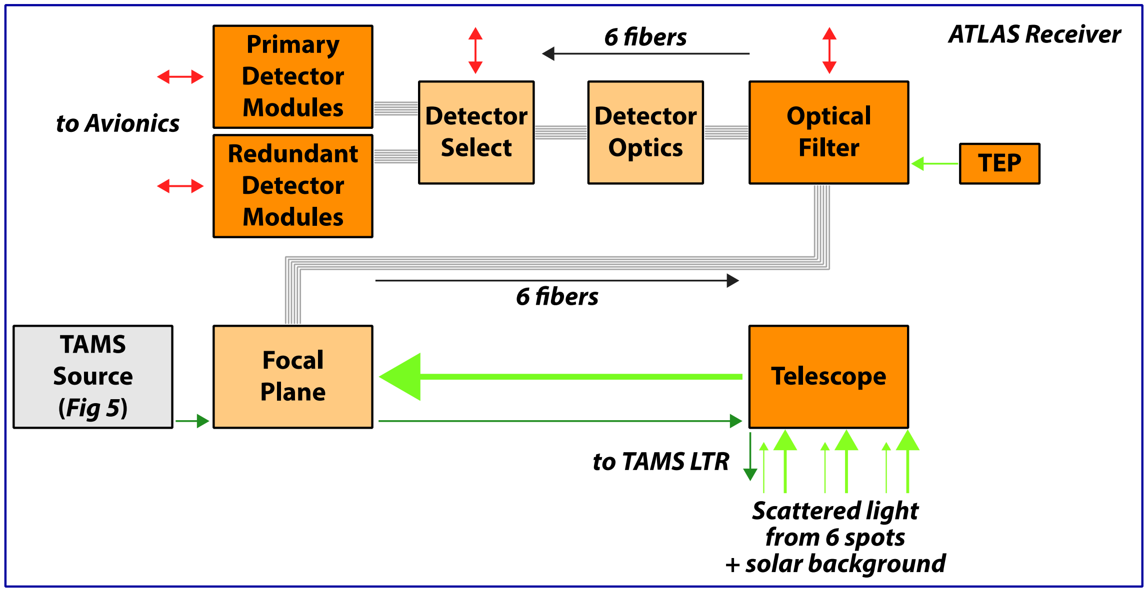


**Figure 3.** Schematic of the ATLAS receiver. Major components described in the text are the Telescope, Optical Fibers, Optical Filters, and Detector Modules. Green arrows denote the optical path; red arrows denote communication and commanding from the ATLAS avionics system; dark green arrows denote the Telescope Alignment and Monitoring System (TAMS) path, which is described in Section 2.1.4 and shown in Figure 5.

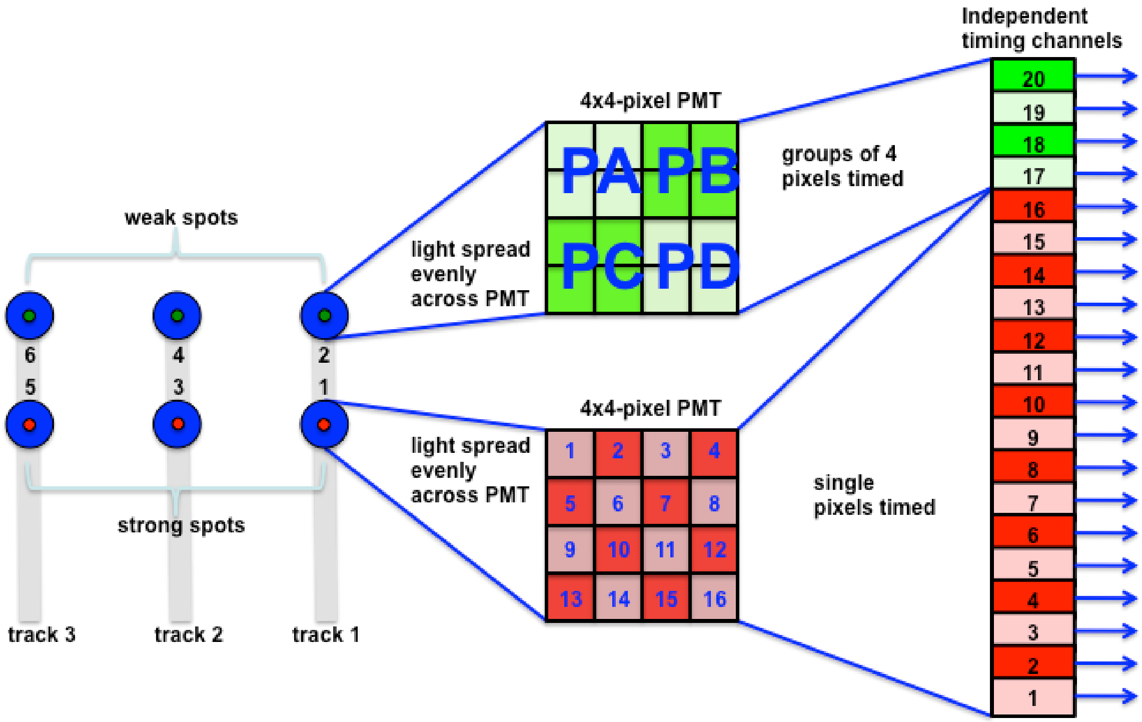


**Figure 4.** Design of the ATLAS multi-pixel photo-multiplier tube configuration for the three weak and three strong beams. Each strong beam uses the 16 pixels (numbered 1 – 16) individually to generate 16 independent electrical outputs, while each weak beam combines four pixels together to effectively create a four-pixel detector (pixels PA, PB, PC, and PD) to generate four independent electrical outputs.

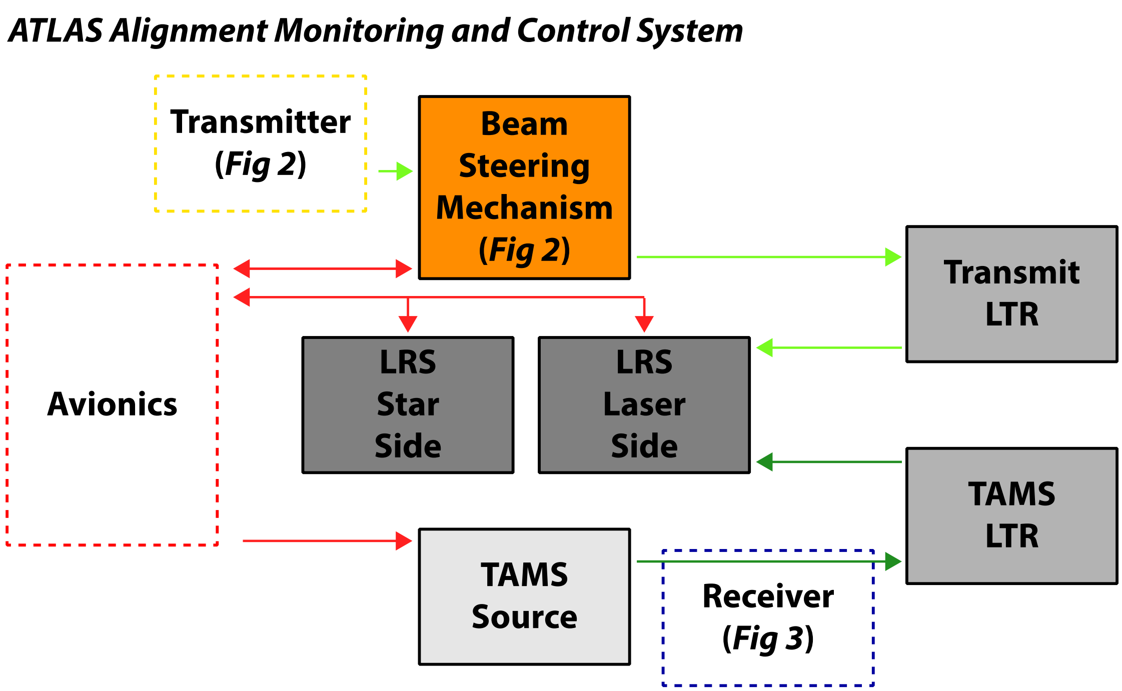


**Figure 5.** Primary components of the ATLAS Alignment Monitoring and Control System (AMCS). The AMCS provides a means to keep the transmitted laser light from the beam steering mechanism (BSM) aligned with the receiver fields of view. Bright green arrows indicate the pathway of 532 nm green light; red arrows indicate power and commanding from the avionics system; dark green arrows indicate the pathway of light from the Telescope Alignment and Monitoring System (TAMS) light source. A portion of the transmitted beams and TAMS beams are routed to the Laser Reference System (LRS) using lateral transmit retroreflectors (LTRs).

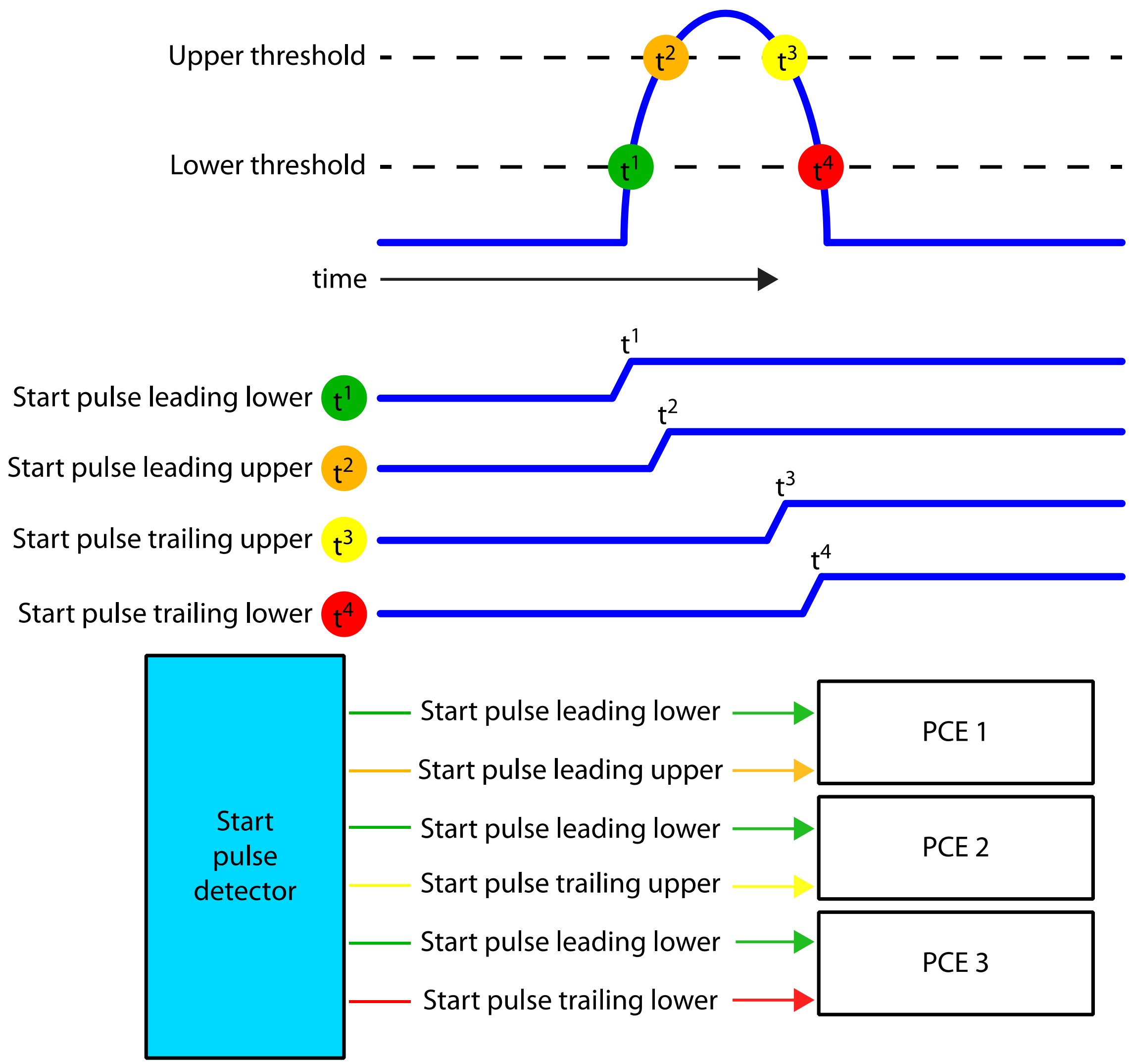


**Figure 6.** The ATLAS start pulse is timed at four places along the transmitted pulse profile. Each PCE card records the time of the leading lower crossing time, as well as one other crossing time. By recording a common event across all cards, the times of events can be aligned.

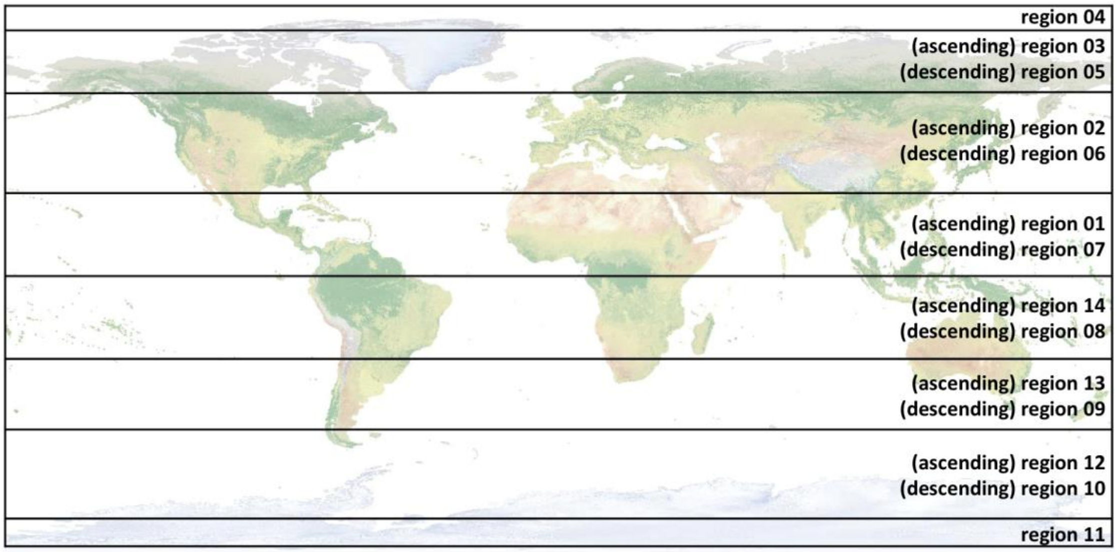


**Figure 7.** ATL03 regions. Region boundaries are used as boundaries between ATL02 data granules. Each complete orbit is broken into 14 distinct granules as indicated.

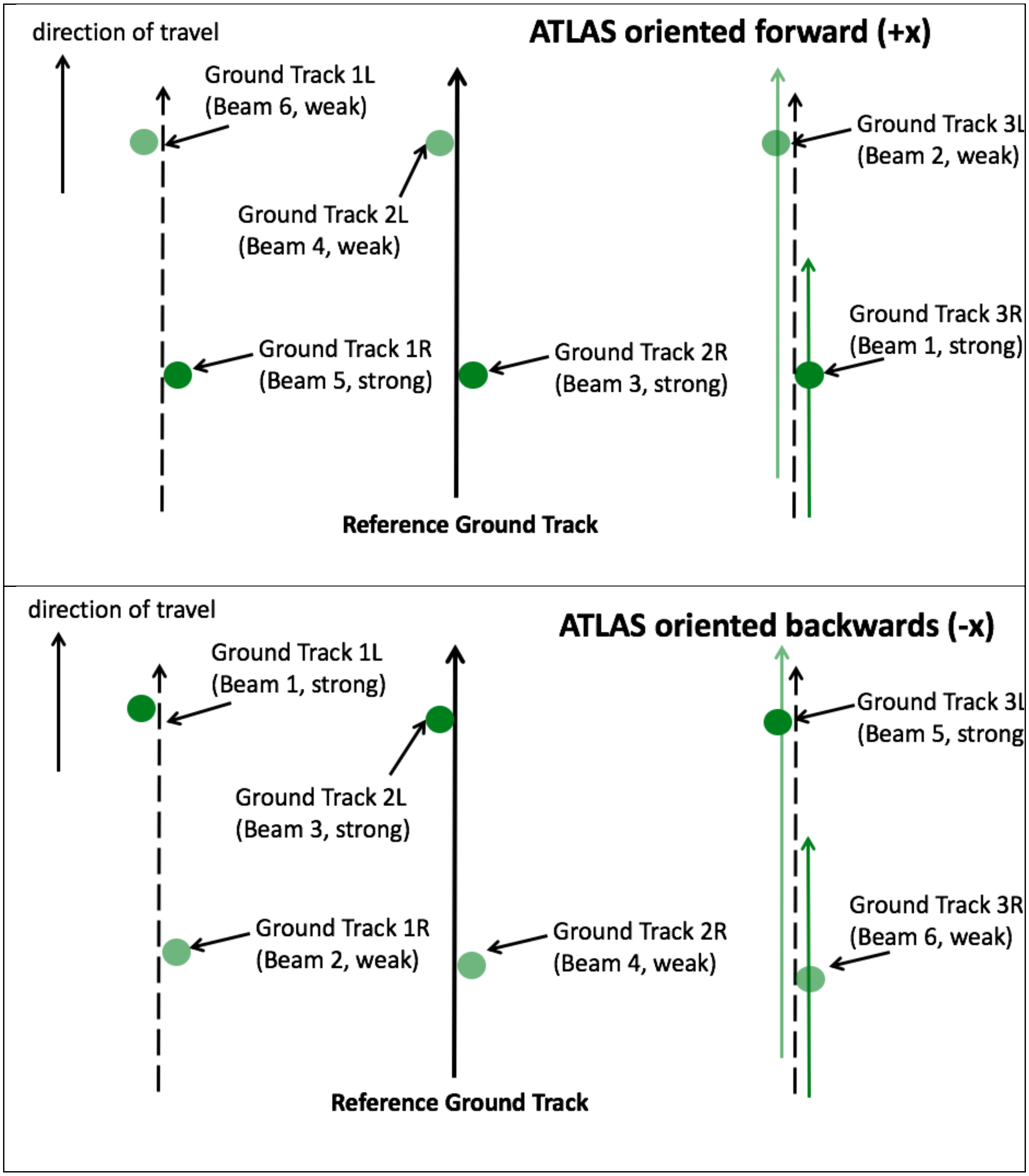


**Figure 8.** The ATLAS beam pattern on the ground changes depending on the orientation of the ICESat-2 observatory. The pattern on top corresponds to traveling in the forward (+x) orientation, while the pattern on the bottom corresponds to

traveling in the backward (-x) orientation.  The numbers indicate the corresponding ATLAS beam, while the L/R mapping are used on the ATL03 and higher-level data products.  The two strong beams with the TEP are ATLAS beams 1 and 3. Derived from Markus et al. (2017), Figure 2.

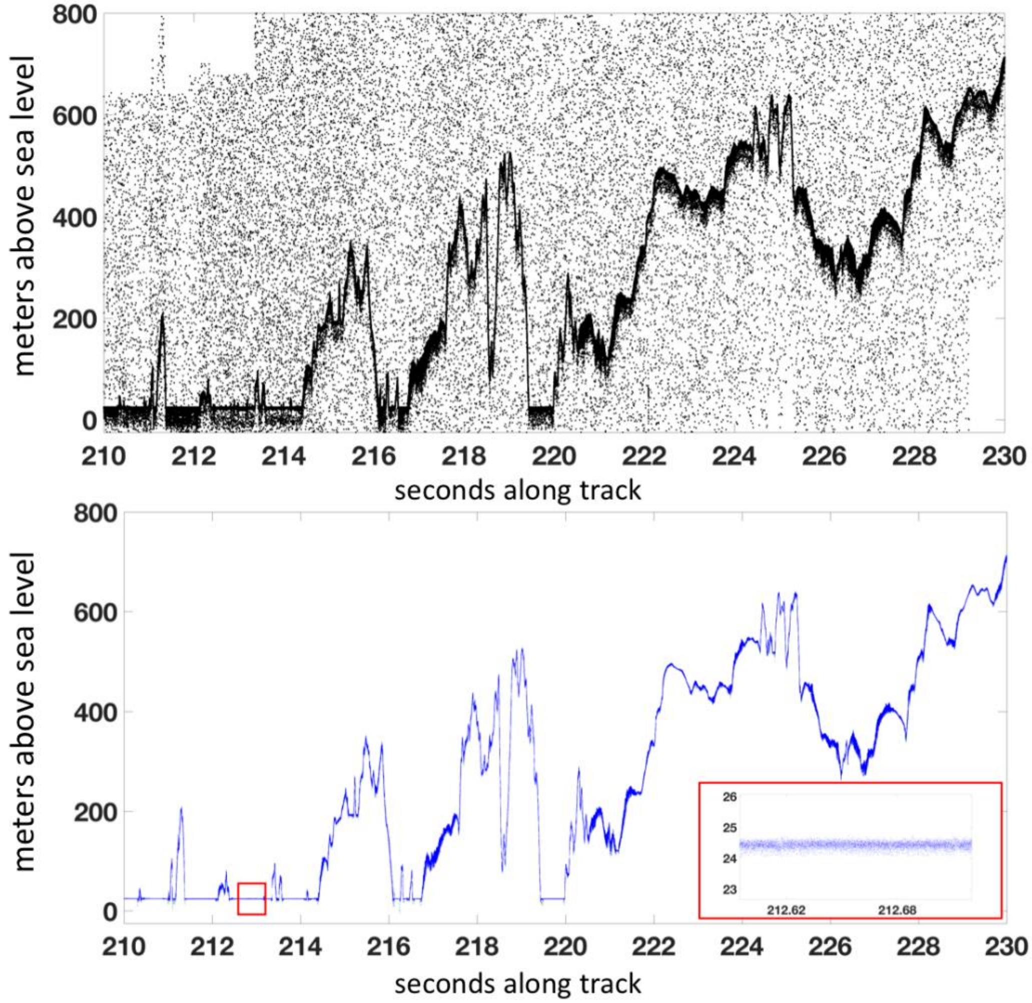


**Figure 9.** Top: Signal and background photons collected by ATLAS over Greenland, 9 November 2018. Bottom: Resulting classification of high-confidence (blue), medium-confidence (red), and low-confidence (green) likely signal photons. Inset shows detail of photon cloud over water surface.

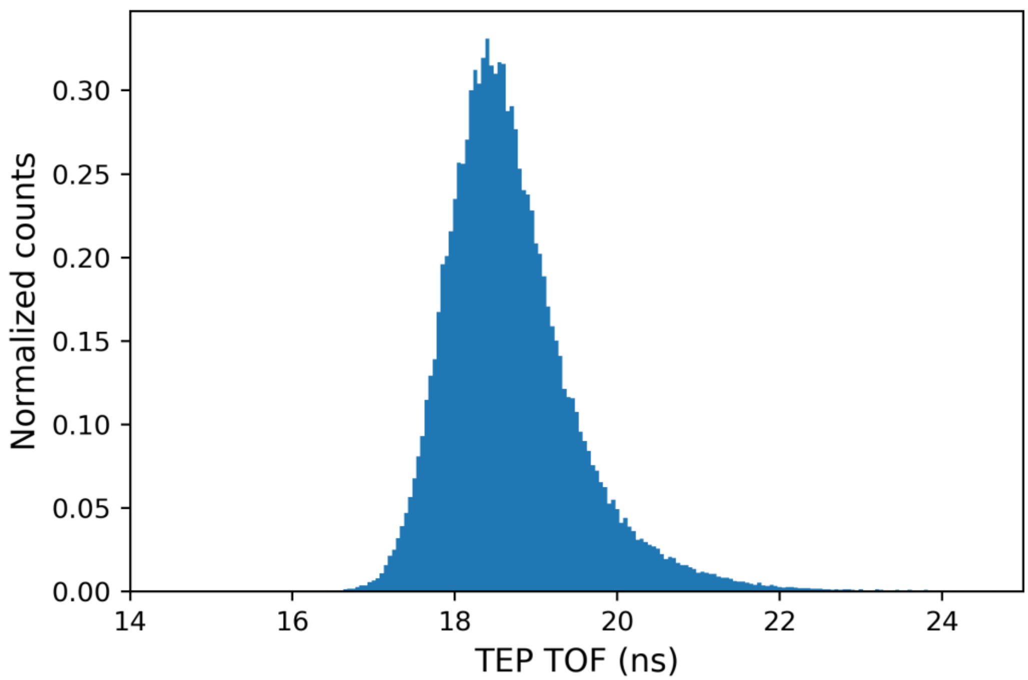


**Figure 10.** A normalized histogram of transmitter echo path (TEP) photons. The x-axis is the TEP photon time of flight (TOF) in nanoseconds, and y-axis is normalized counts. Histogram bins are 50 ps wide, and the histogram is composed of TEP photons from 3,308,000 unique laser fires, or about 300,000 TEP photons.

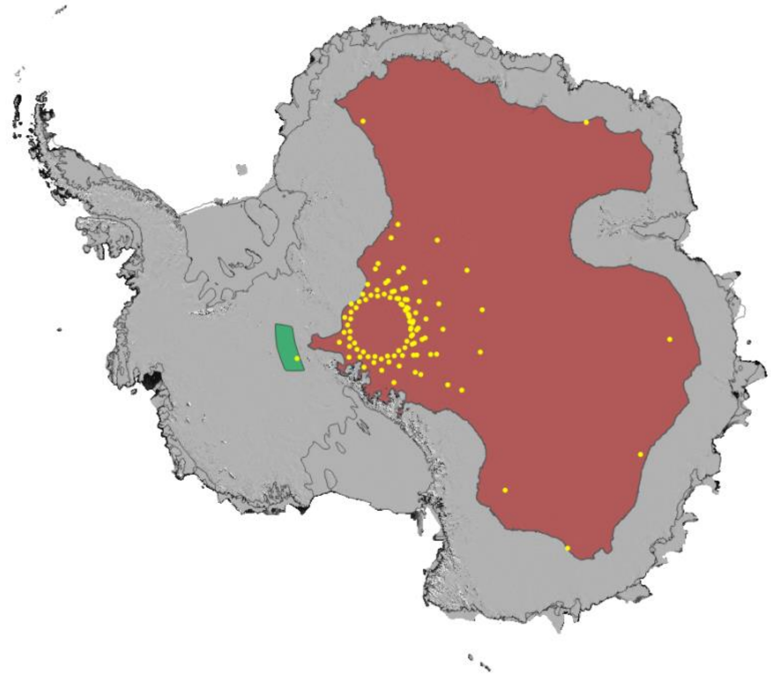

**Figure 11.** Masks used for ICESat-2 crossover analysis. The red and green polygons represent the regions used for the crossover analysis. The red polygon on the East Antarctic Ice Sheet was chosen based on a height mask (2400 m.a.s.l.); the green polygon was added to incorporate some data from the West Antarctic Ice Sheet. The yellow points represent the crossovers that occurred during a single day (there are generally around 100 per day).

**Figure 12.** CCR deployment. Left: a CCR being deployed along the 88S Traverse, with the precise latitude and longitude being surveyed with a GPS. Right: a CCR mounted on the top of a bamboo pole along the 88S Traverse.